COMPUTATIONAL STUDY OF EFFECT OF NANOSECOND ELECTRIC PULSE PARAMETERS ON PLASMA SPECIES GENERATION

by

Nancy Diane Isner

A Thesis

Submitted to the Faculty of Purdue University

In Partial Fulfillment of the Requirements for the degree of

Master of Science

School of Nuclear Engineering

West Lafayette, Indiana

August 2020

THE PURDUE UNIVERSITY GRADUATE SCHOOL
STATEMENT OF COMMITTEE APPROVAL

Dr. Allen Garner, Chair
School of Nuclear Engineering

Dr. Jonathan Poggie
School of Aeronautics and Astronautics

Dr. Tatyana Sizyuk
School of Nuclear Engineering

Approved by:
Dr. Shripad Revankar

To challenging mental health, my cats, and a profound love.

ACKNOWLEDGMENTS

Over the course of three years, here at Purdue University, I cannot adequately begin to convey and fill these pages with all the support that was given to me during this process. Dr. Allen Garner is the first person that comes to mind. I will be forever grateful for the chance I was given and what he saw, to put me in the position I am today. He has given me a mentorship through classwork, navigating the workforce and an understanding the great importance of scientific research. My success in my next journey will be through his teachings, patience, guidance and continued enthusiasm for the work even at the most frustrating of times.

I also would not be where I am without the help of Dr. Jonathan Poggie. Dr. Poggie was instrumental at guiding my research to something of value. If I were to stay in academia, I would want to be a professor like yourself. No matter how or what I was stuck on, you took the time to explain and give me the time process. Continued encouragement and knowing how close I was gave me the strength to keep going.

All of this would not have been possible without the teachings Dr. Tatyana Sizyuk, in my first semester of graduate school. Your jokes and laugh always brightened class. Knowing little to no computational work at the time she fostered me to learn a new language. I know that I still have much to learn, but you are a talented educator, scientist and mentor.

My committee members were instrumental in the final decision of achievement, but all this would not be possible without the team which funded my time here at Purdue University. I would like to acknowledge the NSF/DOE project and the Otto F. and Jenny H. Krauss Scholarship for the financial support. Thank you to Dr. Sally Bane the PI on the NSF/DOE project and showing me the strength and skills to be a boss. I am thankful for the support of the group, including Dr. Carlo Scalo, Dr. Alex Shashurin, Dr. Pavlos Vlachos, Prateek Gupta, Bhavini Singh, Lalit Rajendran, XingXing Wang. Additionally, for the friendship and collaborations with Bang-Shuih Chen. A special thank you goes out to the BEEP group for always listening to research presentation in group meetings, good or bad. I would also like to thank the School of Nuclear Engineering, for my education and to all the faculty and staff that helped with classes, schedules, etc.

I would not be here without the support of my longstanding friends and everyone the I have met here at Purdue University. To my fellow classmates in the Nuclear Engineering department, it was beyond my expectations to transition into a community that has been so helpful toward graduate school and our program. I learned many things from the graduate students ahead of me and the undergraduate students alike. Among my mentors I would especially like to thank Yeni, and Lydia for your support through classes, and your friendship. Nikhil Bharadwaj you are the core and constant in my life. The person who continues to challenge me in life and continues to get me to believe in myself, thank you.

The support of my family has always been steadfast and unconditional. Taking this journey had many unknowns but their belief and trust in me has kept me determined and hopeful. They have given me more than I could ever return. Today an education is important factor in success and is difficult to afford and I am fortunate enough to have the support from my parents. From them I was taught the value of hard work and I hope to embody and translate this throughout my work and my life.

Lastly, to the many more women in science and technology who continue to push the boundaries of social stigma and pursue what drives your passions. You are the continued inspiration. May it be everlasting and inspire others.

TABLE OF CONTENTS

LIST OF TABLES

LIST OF FIGURES

LIST OF ABBREVIATIONS

NPPs-nanosecond pulsed plasmas

PGRS-plasma generated reactive species

EP-electric pulse

CFD-computational fluid dynamics

LTP-low temperature plasma

DC-direct current

AC-alternating current

NS-Navier-Stokes

ACP-atmospheric cold plasma

HVACP-high voltage atmospheric cold plasma

RONS-reactive oxygen and nitrogen species

RF-radio frequency

PRF-pulse repetition frequency

PS-plasma solver

DD-drift-diffusion

LHS-left hand side

RHS-right hand side

1D-one dimensional

2D-two dimensional

LIST OF SYMBOLS

n-plasma density [m^{-3}] or [cm^{-3}]

n_i-ion number density [m^{-3}] or [cm^{-3}]

n_e-electron number density [m^{-3}] or [cm^{-3}]

ϕ-potential [V]

E-electric field [V/m] or [kV/cm]

Γ-species flux [m^{-2} s^{-1}]

μ-species mobility [m^2 V^{-1} s^{-1}]

D-diffusion of species [m^2 s^{-1}]

λ_d-Debye length

α-first ionization coefficient [cm^{-1}]

γ-second ionization coefficient

β-recombination coefficient [cm^3 s^{-1}]

I-current [A]

e-elementary charge [C]

q-species charge [C]

ϵ_0-permittivity of free space

ρ-space charge [C m^{-3}]

p-pressure [Torr] or [Pa]

d-gap length [m] or [cm]

$T_{i,e}$-temperature for ions and electrons [K] or [eV]

k_B-Boltzmann's constant [J/K]

v_s- species velocity [m s^{-1}]

τ-time scale [s]

Λ-characteristic diffusion length [cm]

V_{app}-voltage applied [V]

V_p-voltage peak [V]

σ-pulse width [s]

t_p-time peak [s]

s-sign operator, + for ions and − for electrons

A-area [m^2]

P-power [MW]

Q-energy [MW]

k-reaction rates: one body [s^{-1}], two body [$m^3\ s^{-1}$] or [$cm^3\ s^{-1}$] three body [$m^6\ s^{-1}$] or [$cm^6\ s^{-1}$]

J_t-total current density [C m^{-2}]

J_c-conduction current density [C m^{-2}]

J_d-displacement current density [C m^{-2}]

ν-frequency [MHz]

ρ_m-mass density [kg m^{-3}]

u-flow velocity [m s^{-1}]

τ_s-stress tensor

g-gravitational force

C-collision term

θ-elastic collisions

Ψ-inelastic collisions

ABSTRACT

Multiple industry applications, including combustion, flow control, and medicine, have leveraged nanosecond pulsed plasma (NPP) discharges to create plasma generated reactive species (PGRS). The PGRS are essential to induce plasma-assisted mechanisms, but the rate of generation and permanence of these species remains complex. Many of the mechanisms surrounding plasma discharge have been discovered through experiments, but a consistent challenge of time scales limits the plasma measurements. Thus, a well-constructed model with experimental research will help elucidate complex plasma physics. The motivation of this work is to construct a feasible physical model within the additional numerical times scale limitations and computational resources. This thesis summarizes the development of a one-moment fluid model for NPP discharges, which are applied due to their efficacy in generating ionized and excited species from vacuum to atmospheric pressure.

From a pulsed power perspective, the influence of pulse parameters, such as electric field intensity, pulse shape and repetition rate, are critical; however, the effects of these parameters on PGRS remain incompletely characterized. Here, we assess the influence of pulse conditions on the electric field and PGRS computationally by coupling a quasi-one-dimensional model for a parallel plate geometry, with a Boltzmann solver (BOLSIG+) used to improve plasma species characterization. We first consider a low-pressure gas discharge (3 Torr) using a five-species model for argon. We then extend to a 23 species model with a reduced set of reactions for air chemistry remaining at low pressure. The foundations of a single NPP is first discussed to build upon the analysis of repeating pulses. Because many applications use multiple electric pulses (EPs) the need to examine EP parameters is necessary to optimize ionization and PGRS formation.

The major goal of this study is to understand how the delivered EP parameters scale with the generated species in the plasma. Beginning with a similar scaling study done by Paschen we examine the effects of scaling pressure and gap length when the product remains constant for the two models. This then leads to our study on the relationship of pulsed power for different voltages and pulse widths of EPs. By fixing the energy delivered to the gap for a single pulse we determine that the electron and ion number densities both increased with decreasing pulse duration σ,

however, the rate of this increase of number densities appeared to reach a limit for $\sigma \lesssim 3$ ns. These results suggest the feasibly of achieving comparable outputs using less expensive pulse generators with higher σ and lower peak voltage. Lastly, we study these outcomes when increasing the number of pulses and discuss the effects of pulse repetition and the electron temperature.

Future work will extend this parametric study to different geometries (i.e. pin-to-plate, and pin-to pin) and ultimately incorporate this model into a high-fidelity computational fluid dynamics (CFD) model that may be compared to spectroscopic results under quiescent and flowing conditions will be discussed.

1. INTRODUCTION

Plasmas are the most common state of matter in the universe and have numerous applications due to their specific properties. A plasma is a mixture of charged and neutral particles that has a negligible net charge and exhibits a collective behavior. By applying an external force (e.g. electrostatic or electromagnetic field), alike particles will accumulate together and "collectively" influence the field of motion through long range Coulomb effects. While a plasma is generally described as an ionized gas, not all ionized gasses are plasmas. Although a wood fire can ionize molecules by increasing the temperature, the amount of ionization is insufficient for classification as a plasma. Only at sufficiently high temperatures (~10,000 K) can a flame produce enough ions to be considered a plasma. A plasma must be quasi-neutral, meaning the densities of ion and electron charges will reach approximate equilibrium (i.e. $n_i \approx n_e \approx n$), and n can be treated as the plasma density. Plasmas are highly conductive, can produce high concentrations of energetic species, and are produced by thermal and nonthermal mechanisms. Therefore, plasmas are appealing for a wide variety of applications, including thermonuclear [1], aerodynamic control [2], biological treatments [3], and combustion enhancement,[4] which are discussed in Section 1.2.

Adding energy to a system causes atoms and molecules to gain kinetic energy and collide more rapidly with one another, resulting in the gain or loss of ions. As ionized atoms and molecules interact with free moving electrons, they generate local concentrations of positive and negative charge, inducing a local electric field. The local electric field affects the motion of the particles over large length scales to create the collective behavior [5]. As previously mentioned, the plasma must be macroscopically neutral, except near the electrodes. Beyond the sheath (electron-free zone) there should be no significant space charge in the domain. The plasma criteria are based on the (1) shielding of electrical potentials, (2) total electron density, and (3) collision frequency between electrons and neutral particles [6].

To introduce the concept of shielding, we first define the Debye length. The Debye length, λ_d, is the characteristic distance for the electric field generated by one charged particle to influence another charged particle [6]. Placing a charge (+/-) in a plasma causes a cloud of particles (e.g. electrons/positive ions) to form around the respective opposing charge to create a Debye sphere.

Potentials that exist outside the sphere are shielded by the charged particles. For a plasma to be "quasi-neutral" the dimensions of the plasma must be much larger than the Debye length [6]. Each charge in the plasma interacts only with the charges that lie inside its Debye sphere, so the number of electrons n_e inside the Debye sphere must be very large [6]. The last parameter that helps classify a plasma is the plasma frequency. Plasmas have a body force that acts throughout the system from the generation and charge separation of ions and electrons. The fields that build up act as guides to return the particles to their original positions. Due to the faster moving electrons, the electrons overshoot the slower ions, and this results in the electron plasma frequency. The number of collisions between electrons and neutral particles that induce ionization should not be larger than the electron plasma frequency. The final plasma condition is that the electron-neutral collision frequency must be smaller than the electron plasma frequency [6].

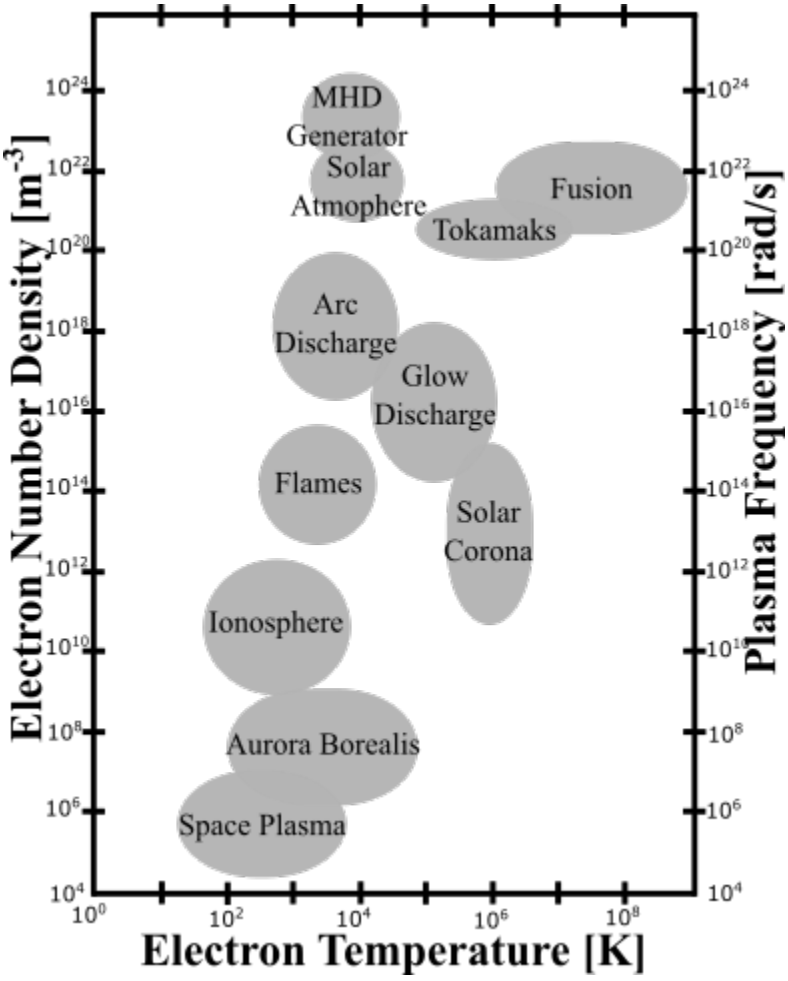

Figure 1.1 Formation of different plasmas based on criteria, based on Bittencourt's decription[6].

The formation of different plasmas depends strongly on the electron number density and plasma frequency as a function of electron temperature, as shown in Figure 1.1. Some naturally occurring plasmas (e.g. space plasma, and aurora borealis) occur at lower temperatures and at a lower electron number density and plasma frequency, while fusion needs high temperatures with a higher electron number density and plasma frequency. In contrast, laboratory plasmas (e.g. glow discharges, and arc discharges) occur around an electron temperature of 11604 K with a sufficiently high electron number density and plasma frequency. In general, a plasma can form with either the input of thermal or electrical energy. A thermal, or hot, plasma occurs when the increased ion temperature equals the electron temperature, reaching a state of equilibrium. Lightning is a simple observable state of a thermal plasma. Preceding a lightning strike, electrons are moving at such a high velocity that collisions rapidly accelerate ions until large clouds of negative and positive charge form. Once a conductive bridge is formed, the electrical reaction produces the light, energy and heat we know as lightning. Other examples of thermal plasmas include arc circuit breakers, arc welding, and plasma cutting [7]. In contrast, a non-equilibrium, or cold, plasma can occur when a strong electric field is applied, and the ion temperature is significantly lower than the electron temperature. Non-equilibrium plasmas typically are referred to as low temperature plasmas (LTPs) because they produce limited thermal energy. Examples of LTPs include dielectric barrier discharges (DBD), plasmas actuators, and plasma jets [2,8,9]. Specifically, these plasmas have become increasingly popular in medicine and the food industry, as discussed in more detail in Section 1.2.3. It is worth mentioning the various ways in which plasmas are generated, because this thesis focuses on low temperature gas discharges.

LTPs have become important for numerous applications in combustion, flow control, and medicine over the past decade. Section 1.1 introduces gas discharges and their behavior, including how circuit design, gas state, and electric pulse (EP) parameters influence species generation (i.e. ions and electrons). Section 1.2 also summarizes the applications of gas discharges and Section 1.3 discusses the various models and numerical approaches for predicting their behavior.

1.1 The Basics-Gas Discharge

A gas discharge occurs when a sufficiently strong electrical potential is applied to a gaseous medium [10]. The invention of the gas-discharge tube [11] facilitated plasma visualization and characterization. A gas discharge may be divided into three distinct types depending upon the relationship between voltage and current: dark, glow, and arc discharges. This review of gas discharge will focus on direct current (DC) discharges. Although, this thesis focuses on nanosecond pulsed plasma (NPP) discharges, which modifies the spectrum shown in Figure 1.2(b), the mechanisms and concepts will be similar. Nevertheless, this review is sufficient for a basic understanding.

1.1.1 DC discharge

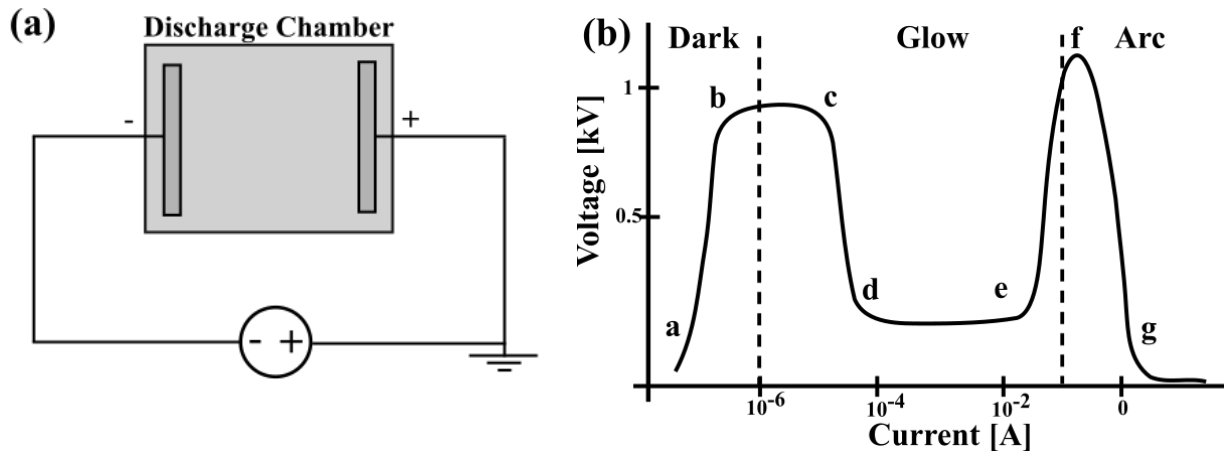

Figure 1.2 (a) Circuit diagram for a discharge chamber. (b) Voltage as a function of current for a DC discharge.

The DC discharge is the simplest reproducible discharge. The typical system consists of two electrodes and a voltage source, shown in Figure 1.2(a). The space between the electrodes is usually sealed (e.g., vacuum tube) and maintained at a low pressure (0.1-10 Torr). The interelectrode gap distance and the gas pressure of the gas play an important role in determining when the plasma becomes conductive, which typically scales with the product of pressure and gap distance. The chamber is typically filed with noble gasses and exposed to an applied potential of a

few hundreds or thousands of volts. Factors such as circuit design will affect the discharge profile with the discharge type typically determined from the calculated current.

Figure 1.2(b) shows the three main regimes as the dark discharge, glow discharge and arc discharge. Although the results depend on the characteristics of the external circuits, a Townsend or dark discharge generally occurs when the current is less than 10^{-6} A, a glow discharge occurs when the current is between 10^{-6} A – 10^{-1} A, and an arc discharge occurs when the current is greater than 10^{-1} A. [10]. The voltage/current plot shows the complex nature and the nonlinearity of the gas discharge phenomenon. The concomitant region transitions and ion-electronic properties will be discussed.

Conduction requires a gradient of electrical potential created by the charged particles in the domain. Process initiation requires the presence of some free electrons. Initially, at low voltages, the current is generated by low levels of ionizing radiation shown in Figure 1.2(b) at point (a). The current will saturate from (a-b); as the voltage increases, the free electrons in the domain accelerate and collide with other ions and neutrals [12]. The interaction of a single electron with a neutral particle deposits energy and ionizes the neutral particle, creating an additional electron. This second electron is now free to move and collide with other particles. The number of charged particles begins to increase exponentially, and this phenomenon is called the Townsend avalanche [13].

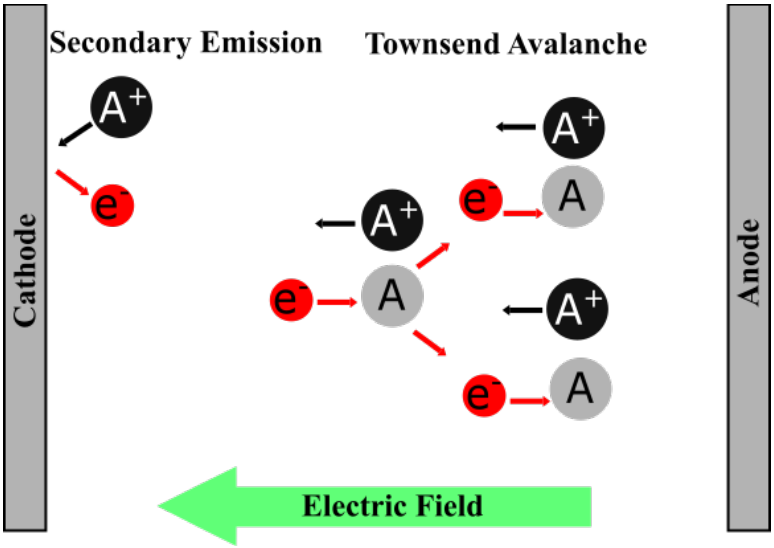

Figure 1.3 Ball and stick model of first and secondary ionization coefficients

Townsend represented this concept as the first ionization coefficient α, which is the number of electrons produced per one electron travelling per unit length [14]. This assumes that a single electron strikes particles in a linear progression, as represented in Figure 1.3. The electron and neutral particles collide to produce one ion and two electrons. Additionally, electrons can also be emitted into the domain from ion bombardment. An ion will strike the cathode and emit a secondary electron. This process is characterized by Townsend's second ionization coefficient, γ [13]. At point (b), Townsend avalanche has begun and current begins to increase while voltage remains steady. The combination of Townsend avalanche and secondary emission causes the current to increase exponentially, such that the plasma becomes self-conducting at point (c). The total current I at the anode $x = d$ including both Townsend avalanche and secondary emission is given by [14]

$$I = \frac{I_0 e^{\alpha d}}{1 - \gamma(e^{\alpha d} - 1)}, \tag{1.1}$$

where I_0 is the current at the cathode. Equation 1.1 shows that I depends on the first and second ionization coefficients, and altering the gap distance changes the probability of collision with another molecule. While the mean free path depends on the local gas state, the distance between electrodes would affect the collision frequency. Reducing gap size causes more collisions to occur to excite and ionize the gas particles. Pressure also affects the mean free path, in which at a high or low pressure the velocity of particles is perturbed. Paschen studied the effects of varying pressure and distance and obtained a relationship describing the necessary voltage to achieve breakdown. Paschen's Law describes the breakdown voltage V_b as a function of the product of pressure p and gap length d as [15]

$$V_b = \frac{Bpd}{\ln\left(\frac{Apd}{\ln(1+\gamma^{-1})}\right)} = \frac{Bpd}{\ln(Apd) - \ln(\ln(1+\gamma^{-1}))}, \tag{1.2}$$

where A and B are experimental quantities determined over a restrictive range of electric field/pressure (E/p) values for a given gas [16]. These parameters were obtained for classical discharge experiments for centimeter or millimeter gap distances [17]; however, the physical

phenomena changes for microscale gap distances at atmospheric pressure [18–20]. In this case, the small gap distances lead to sufficiently strong electric fields that strip electrons from the cathode through field emission [18–20]. These electrons ionize the gas molecules near the cathode to create a region of positive space charge that induces a second contribution to the secondary emission coefficient and the cathode electric field that gives field emission current density. Thus, this ion-enhanced field emission drives breakdown at these gap distances that are too small for avalanche to dominate. Mathematically, asymptotic analyses show that the minimum voltage predicted by Paschen's law ($V_{b,min}$ at a certain pd) may be eliminated and the breakdown voltage scales linearly with voltage at sufficiently small gap size [16]. Interestingly, for certain electrode conditions (work function and field enhancement), the minimum may occur and the linear decrease in breakdown voltage may occur *after* the Paschen minimum [21]. In either event, this linear scaling is important when considering device reliability for micro- and nano-scale electronics since the breakdown voltage decreases with decreasing size rather than increasing with decreasing voltage, as predicted by Paschen's law.

Before breakdown, the number densities remain small and the electric field remains unaffected by space charge. At breakdown (point c), Townsend avalanche and secondary emission have generated enough charged particles and space charge to affect the electric field. A separation of the heavier ions and lighter electrons forms the positive and negative sheaths. A local concentration of positive ions at the cathode forms to initiate the voltage drop. The voltage drop (c-d) is highly unstable and makes numerical calculations difficult later. The voltage drop initiates the transition to achieve glow.

After stabilization (d-e), the voltage becomes independent of current and normal glow is achieved. Initially, in normal glow, the electrode current density is independent of the total current. Only a small surface area of the electrode is transferring current, with a larger surface area used with increasing total current. This pushes the cathode current density above a natural state and the potential starts to increase significantly. From (e-f), the sharp increase is recognized as abnormal glow. The discharge now has high levels of voltage and current, leading to the transition into the arc discharge regime.

The transition from glow to arc is represented by section (f-g), where the voltage decreases with increased current. Arc discharges are in thermal equilibrium and the key mechanisms of electron emission are thermionic emission, field emission, and thermal ionization. There is substantial thermal output from Joule heating, in which the arc could shatter the gas tube. Although vacuum arcs can be formed in vacuum tubes, arc discharges are generally formed at high pressure. Hot gas-tubes were developed to handle the higher currents that arcs generate (e.g. mercury-arc rectifier, spark gap, ignitron, thyraton) [6]. After the transition, the voltage slowly begins to increase again as current increases and an arc is sustained after this point.

In a constant electric field at low pressure (~760 mTorr), the Townsend, glow, and arc discharges are the most common discharge types formed. Figure 1.2(b) does not show other profiles which can form at higher pressure (~760 Torr). Some examples of high-pressure non-equilibrium discharges are corona, dielectric barrier, and streamer discharges. Plasmas at atmospheric and higher pressures require a larger input voltage to overcome voltage breakdown. Corona discharges can overcome this by using sharp electrode tips with large curvature to enhance the electric field at the tip, which can exceed the dielectric strength of the conductor and ionize the surrounding air to initiate electrical breakdown. A common technique used to prevent arcing across small gaps is to add a dielectric barrier, which reduces the electric field by shielding the charged particles. This resembles the phenomena involved in a streamer discharge, although shielding occurs in the bulk gas rather than close to the electrode. In a polarized avalanche, electrons will group toward the head of the streamer and ions will group toward the tail. The large electron head can now shield the electric field to prevent arcing.

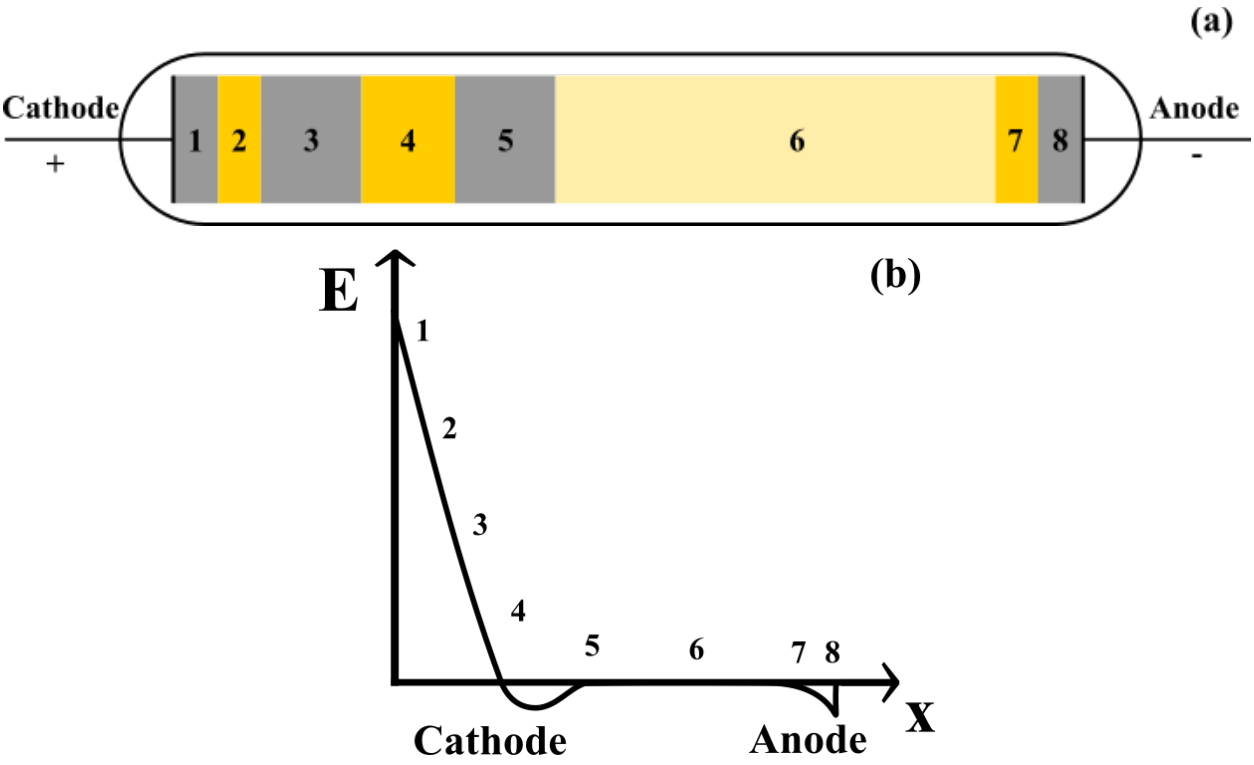

Figure 1.4(a) Column arrangement showing different regions for a gas discharge, (b) Qualitative representation of the electric field strength in the column over a given space.

1.1.2 Glow Discharge Column

The glow discharge column in Figure 1.4(a) has eight distinct regions. Ion-electron emission from the cathode surface provides the source of electrons to maintain a glow discharge. Initially, the electrons emitted from the surface have low energy (~1 eV), which cannot excite other nearby atoms and molecules. This is region 1, called the Aston dark space, in which no light is emitted directly next to the cathode. Near the cathode, the electric field is strong, and the electrons gain energy to start exciting other molecules. This is short lived as the excited atoms quickly return to ground state; however, they do expel radiative energy in the form of a photon. The photon at a given wavelength produces a soft light referred to as the cathode glow (region 2). As more electrons move and gain energy, they excite molecules and cause impact ionization reactions, which starts the avalanche process. No additional light is produced from the ionization reactions in region 3, the cathode dark space, where the voltage drop occurs. Enough collisions have now occurred to increase the electron number density significantly, but the electrons are pulled to

recombine with positive ions and light is given off in the form of bremsstrahlung radiation. This appears as an intense light in region 4, the negative glow region. Electrons continue to lose energy and recombine with ions, resulting in region 5, the Faraday dark space. All the regions from the Aston dark space (region 1) to the Faraday dark space (region 5) comprise the cathode layer.

The largest section of the tube is region 6, the positive column. The plasma has reached a state of quasi-neutrality where the electric field remains low and the electrons have gained their average amount of kinetic energy. The final two regions are observed in the anode layer. Ions are repelled from the anode, pushing the electrons into the region of anode glow, region 7, where the remaining few excitation reactions produce what little light remains. The energy of electrons continues to decrease, which results in region 8, the last dark space.

Figure 1.4(b) shows the electric field strength in the column. The sharp gradient and proximity of regions 1 through 5 make it the most difficult to handle for theoretical and computational descriptions. The eight regions have been described with distinct properties, but this is clearly a continuum of mechanisms rather than several distinct ones. A complete plasma model requires tracking all particle locations and velocities. Each region would have significant restrictions imposed to account for all the physics, which would vastly increase the computational cost. To simplify the computational approach and reduce expense, the column may be represented by three distinct regions: the cathode layer (regions 1–5), the positive column (region 6), and the anode layer (regions 7 and 8). Different methods are employed for model development, in which some remain costly to capture the physics and others are simplified to make them computationally practical. Section 1.3 discusses the differences and challenges for simplified models verse detailed models.

1.2 Plasma Applications for LTPs

Plasma science and technology have made many advances throughout the years and now play a role in a large range of industrial applications. The 2017 Plasma Roadmap [7] gives the most current and comprehensive list of current plasma applications. With the integration of plasma properties, industry has advanced the fields of oil and gas, aerospace, medicine and material processing. Because this thesis focuses on developing a computational tool for characterizing such plasmas,

this section briefly summarizes the benefits and challenges surrounding atmospheric pressure LTPs, focusing on combustion and ignition enhancement, flow control, and biological treatments.

1.2.1 Plasma-assisted combustion and ignition

Improved fuel consumption has always been at the forefront of the energy industry [22]. Over the past decade, multiple countries have imposed new regulations for emissions, leading to new approaches for engine development [22]. An alternative option for industries has been the use of nonequilibrium plasmas for improving fuel efficiency while minimizing cost [23]. Starikvoskiy and Alexandrov [22] considered the application of nonequilibrium plasmas to improve ignition delay, increases flame speed and stability, and enhances mixing stability of air to fuel ratio for internal combustion and hypersonic engines. Numerous fuels and discharge conditions have been studied to understand the mechanisms surrounding plasma assisted combustion and ignition. Broadly speaking, plasma induced phenomena are generally divided between thermal characteristics and nonthermal characteristics. Thermal mechanisms include homogenous and inhomogeneous gas heating from energy released to increase chemical reactions rates and perturb the flow to induce more turbulence and mixing. Nonthermal mechanisms include increased plasma generated reactive species (PGRS), altered kinetic pathways and diffusion processes, and the production of ionic wind due to the accumulation of space charge in the gas. Ionic wind, which comes from momentum transfer between species, is an important mechanism that can enhance combustion. The movement of ions will change the local flow velocity which aims to increase flow turbulization and mixing [24].

Recent studies have developed predictive models for these mechanisms. Adamovich addressed some of the key challenges in modeling nonthermal effects from a kinetic perspective [25]. The dominant energy transfer and chemical reaction processes for modeling complex hydrocarbons are not fully understood [25]. Predictions must be made to understand ignition in a low temperature plasma. This requires knowing reaction rates such as electron impact ionization, dissociation of air and hydrocarbons, vibrational relaxation, quenching of excited electron states, and reactions between excited states. Many of these reactions have been studied at high temperature, but the data from these reactions does not always correlate to LTP experiments or models. Some chemistry mechanisms are less sensitive to temperature but others remain sensitive. Konnov's [26] high

temperature mechanisms agreed well in low temperature experiments and kinetic modeling of H_2-air, CH_4-air, and C_2H_4-air [27] but did not agree with experiments and modeling of C_3H_8-air. Increasing hydrocarbon complexity necessitates more elaborate mechanisms.

Modeling air-fuel ratios is complicated since a complete model would have to represent all the species and all the associated reactions, making the highest fidelity model impossibly computationally expensive. To ease this burden, simulations often use reduced sets of reactions obtained from steady state approximations and validate these models within a relative error. Since the PGRS alter the combustion dynamics, they also change the flame, which behaves dynamically. Flames are typically considered as fluids (i.e. gas or liquid), which are studied widely throughout physics and often represented mathematically using the Navier-Stokes (NS) equations.

NS equations are a representation of the collective behavior of a large system of interacting neutral particles. The equations are well understood to be the fundamental representation of a fluid because they uphold the conservation laws. A general form of the balance equations that describe conservation of mass, momentum and energy are given by [28].

$$\frac{\partial \rho_m}{\partial t} = -\nabla \cdot (\rho_m \vec{u}), \tag{1.3}$$

$$\frac{\partial \rho_m \vec{u}}{\partial t} = -\nabla \cdot (\rho_m \vec{u}\vec{u}) - \nabla p - \nabla \cdot \boldsymbol{\tau_s} + \rho_m \vec{g}, \tag{1.4}$$

and

$$\frac{\partial}{\partial t}\left(\frac{\rho_m u^2}{2}\right) = -\nabla \cdot \left(\frac{\rho_m u^2 \vec{u}}{2}\right) - (\vec{u} \cdot \nabla p) - (\vec{u} \cdot [\nabla \cdot \boldsymbol{\tau_s}]\,) + p(\vec{g} \cdot \vec{u}), \tag{1.5}$$

respectively, where ρ_m is the mass density, u is the flow velocity, p is the pressure, $\tau_s$is the stress tensor, and g is the gravitational body force. These equations govern fluid movement when the fluid density and viscosity is considered in the tensor term. The NS equations are extremely complex and currently remain a challenging millennium problem [29]. Simplifications and assumptions, such as solving for a steady state or neglecting viscous forces, are made to

characterize the behavior of the fluid. No fluid is ever truly inviscid; however, for some flows, viscous forces are only important near the boundaries.

Information about the excited and ionized species is not obtained from the flow solver, which requires the plasma chemistry model. Coupled models will include mass conservation and force equations for each species and conservation of momentum. Since the plasma model and flow model occur on different timescales, incorporating the two models creates a large computational requirement. The time and length scales for the plasma discharge are discussed in Section 1.3.1.

1.2.2 Flow Control Applications

In aeronautics and astronautics, companies are continuing to improve flight systems for commercial and defense applications. The focus is on improving safety and reducing fuel consumption of aircraft and aircraft engines. Simply stated, flow control is enacting and manipulating flow to obtain a desired change [2]. Flow control devices are used to increase efficacy in areas that delay stall, increase lift, and decrease drag for an aircraft. Unsteadiness in flow is typically seen or heard when an aircraft vibrates and makes noise. One can conclude that energy is being lost to the system. Flow control devices seek to counteract the energy losses.

Plasma actuators are currently a popular technology for aerodynamic flow control. The plasma actuator is a form of active flow control, which requires an energy input to work. These devices have since risen to the forefront of the field because they are easy to turn on and off and operate over wide frequency ranges with few moving parts. Important benefits include delaying the transition from laminar to turbulent flow, reducing separation, and improving shock patterns. The plasma actuator accomplishes this by altering the boundary layer characteristics.

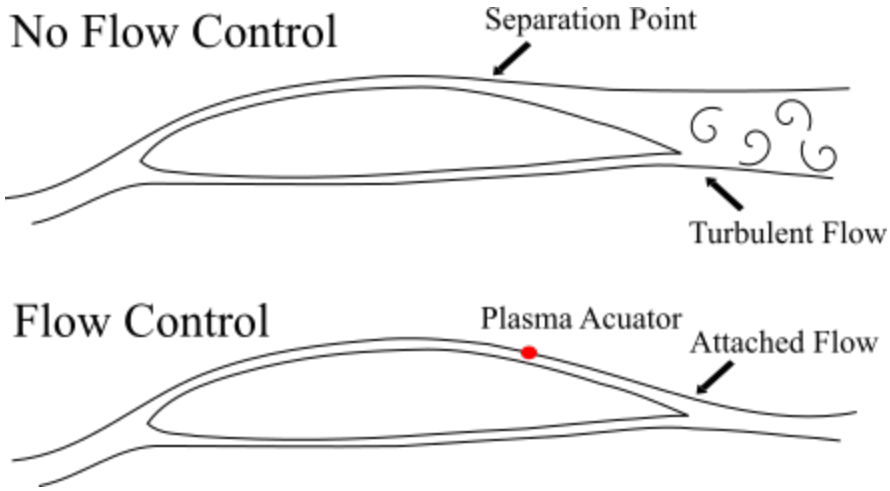

Figure 1.5 Boundary layer conditions with the use of a plasma actuator

Figure 1.5 shows the formation and detachment of streamlines from the surface of a flying object. Without flow control, the transition point from laminar to turbulent flow comes earlier and large areas of separation from the boundary layer start to form. Adding an actuator at the transition point delays the separation of the boundary layer [30]. The plasma induces a body force to align the flow; and the subsequent plasma heating further increases momentum.

The mechanisms involved in plasma combustion resemble those for modeling plasma and flow. Both involve gas heating caused by interactions of the flow and energy relaxation in the plasma. The PGRS still alter the flux and kinetic pathways and the momentum produces an ionic wind. Thus, similar challenges arise when developing models or conducting experiments using a flow control device. The plasma actuator alters the flow around an aircraft wing or a flying object and must now be coupled to a flow solver to gain comprehensive understanding of the fluid dynamics and the chemistry. This is an ongoing effort among many groups to create a high fidelity model that can couple the timescales of the plasma to the flow [31].

1.2.3 Medicine and Biology

Atmospheric cold plasmas (ACPs) are well established in medicine, food and water sterilization, and other biological applications [3,9,32]. Nonequilibrium plasmas have effectively inactivated bacteria in biological media [33–36] without harming healthy cells. In medicine, ACP treatments are

implemented to disinfect equipment, combat bacterial and fungal diseases, palliate chronic wounds, and rejuvenate epidermal tissue [3]. Applications in food and water treatment use ACPs to decontaminate different physical states (i.e. solid, liquid, or semi-solid), and sterilize packages [37–40]. In addition to their effectiveness, ACPs are also low risk and low cost with easy handling and maintenance [41,42].

The germicidal effects of ACPs arise because of the increased amount of PGRS from electron-impact reactions [43]. An example of this is the generation of ozone, which restricts cellular respiration and is also known to have enhanced bactericidal effects. Furthermore, it has been suggested that charged particles play a significant role in the rupture of the outer membrane of bacterial cells [43]. A limitation of ACPs include poor electron and ion permeability into the bulk [3,44]. Using ACPs to treat food requires leveraging excited and ionized particles to enhance microorganism inactivation on food surfaces [43].

Common ACP experiments with biological interactions are typically designed as dielectric barrier discharges, plasma jets, or plasma arrays [45]. High voltage ACPs (HVACPs) have effectively inactivated microorganisms on surfaces in solids and liquids [3,36,43]. While successful, much remains unknown about the reactive oxygen and nitrogen species (RONS) diffusion process, ion permeability, and subsequent relationship that effects the sterilization and modification of cellular processes. Many studies have focused on improving the penetration depth of the RONS by optimizing the plasma chemistry [44]. The transition from the gas to liquid bulk is complex, with a plethora of species and processes to consider. This increases the challenges of developing a predictive model, whether examining the direct/indirect or hybrid plasma interaction or the mass transfer from the gas-liquid boundary [32,44,45].

1.2.4 Nanosecond Pulsed Plasma (NPP)

The previous section discuss how plasma technology has greatly improved multiple industrial applications, such as combustion [4], flow control [2] and medicine [3]. These advances in plasma technology have come from the development of nanosecond pulsed plasmas (NPP), whose generation of non-equilibrium plasma at atmospheric pressure makes them attractive for numerous applications [46]. Particularly, the low duty cycle of NPPs makes them more efficient at generating

ionized and excited species than DC or AC driven plasmas [47] . The high voltage and strong electric fields are well suited for this work but can prove challenging to model. Furthermore, the shorter duration pulses and faster rise times are more efficient in producing PGRS than longer duration pulses with slower rise times [48]. Shorter pulses increase the mean electron energy, which increases the electron energy density function (EEDF). The increase in energy means the electrons can deposit more energy in an electron-neutral reaction and ionizes more particles in total. Additionally, the nature of repetitive pulsing is useful because the energy input required to reach a steady state is lower than using a constant source. The recent popularity of these plasmas motivated more experiments to characterize and measure their properties. While experiments have assessed many of the mechanisms surrounding plasma discharge, short timescales limit plasma measurements. Coupling a well-defined model to experimental research will help elucidate complex plasma physics.

Model development typically begins at lower pressure since it is easier to obtain a diffuse homogenous plasma. Park and Economu [49] applied a fluid model to radio frequency (RF) pulses at low pressures (0.5-2 Torr) to show that the electron density profile becomes flatter in the bulk plasma and the sheath thickness decreases with increasing pressure. The electron temperature peaks near the plasma sheath and begins to decrease thereafter. Increasing the pressure also necessitated finer grids, dramatically increasing computation expense; therefore, although recent experimental work demonstrated the utility of atmospheric pressure plasmas for multiple applications [47,48,50 51], computational studies for these conditions remain complicated.

NPPs were investigated by Stark and Schoenbach [51] for electron heating at atmospheric pressure, while Pai and others studied conditions at atmospheric pressure such as the pulse repetition frequency (PRF) (1-30 kHz), the inner electrode distance (0.5-10 mm), and the ambient gas temperature (300-1000 K) on the discharge [52–54]. The interest in repetitive pulsing arises from the production and accumulation metastable species important for sustaining the discharge and using the active species for plasma applications. This is possible because the pulsed discharge can reach higher values of the reduced electric field compared to DC or AC discharges [47].

Experiments and modeling in this field have progressed significantly over the past twenty years. Efforts by Kushner [55] and Poggie [56] have led to major accomplishments in fluid, kinetic and hybrid

modeling. Improvements have included better approximations to Boltzmann's equation, better characterization of reactions for specific applications, and improved numerical techniques. Much room remains for improvement. Plasma modeling continues to encounter difficulties with the enormous differences in time and length scales and the lack of transport and swarm parameters. The nonlinearity of the problem increases computational challenges by compounding many numerical instabilities. Different models and numerical techniques have been developed and we will summarize the differences and the challenges in the next section. Choosing a model that is appropriate and achievable for the specific application is imperative. This thesis aims to create a feasible physical model within the numerical limitations of timescales and computational resources.

1.3 Numerical Efforts

The prior sections outline the physics and industrial applications of gas discharges. This section details the numerical efforts, techniques, and challenges for solving this problem computationally. While different experimental discharge data are readily available [22,51–53] , the details of the initial moments of the discharge are not completely visible and not easily explained. Thus, different modeling approaches elucidate more of the beginning physics and provide a more complete picture. As previously stated, an ideal model would track all particles; however, such a model is impossible to solve with today's computing power. Simplifications and assumptions must be made to adapt to the current challenges.

1.3.1 Plasma Modeling Challenges

A large challenge to overcome in plasma modeling are the timescales that occur within the plasma discharge. The fundamental mechanisms of interaction between charged and neutral particles such as ionization, drift, diffusion, and recombination, operate on different timescales. Each timescale will be defined to show how each process will differ. An example calculation from a discharge simulation will show the disparities between positions in the plasma (i.e. cathode sheath and positive column) and the electron and ion swarm parameters. The electric field and gas state will alter with position when moving throughout the domain because each solution is unique.

The simulation uses the one-dimensional drift-diffusion (DD) equations for two species (i.e. electrons and ions (N_2^+)). The solution replicated Adamovich's nanosecond pulsed discharge simulation with a dielectric barrier [46]. To represent the source terms in the governing equations, we used Townsend's ionization model and recombination. The governing equations were then coupled to Poisson's equation to solve for the electrostatics, as described in more detail in Chapter 2. Figure 1.6(a) shows the discharge configuration, where including the dielectric barrier (in red) increased the capacitance. Discharge simulations were performed at 60 Torr, a 1 cm gap, a 1.75 mm dielectric with a relative permittivity of 4.3 and an applied voltage of 20 kV. The electric field and number densities of the ions and electrons are shown in Figure 1.6(b).

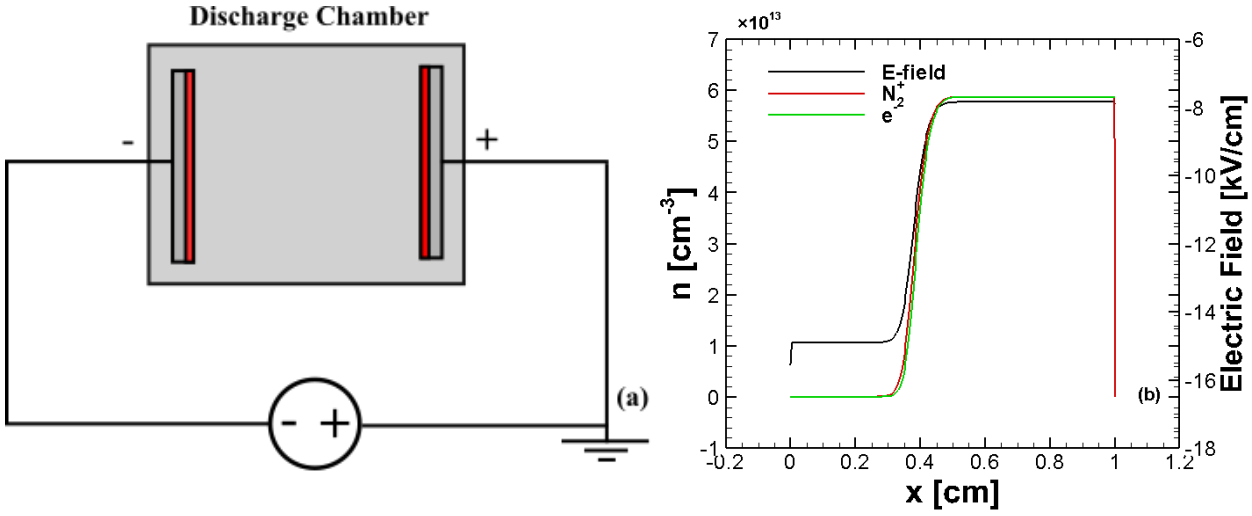

Figure 1.6 (a) Discharge geometry with the inculsion of a DBD in red; (b) Nanosecond pulse discharge simulation for N_2 with a dielectric barrier at 60 Torr and a peak voltage at 20 kV.

For drift, we first define the drift velocity of the charged particles which is determined as $\boldsymbol{v_{dr,s}} = \mu_s \boldsymbol{E}$. This makes the timescale for drift simply $\tau_{dr,s} = d/|\boldsymbol{v_{dr,s}}|$ for each species. The size of the cathode sheath is $d_{cs} \approx 0.2\ cm$ and the positive column is $d_{pc} \approx 0.8\ cm$. The magnitude of the electric field in the cathode sheath is about 15,000 V/cm and in the positive column is about 8000 V/cm. The diffusion coefficient is obtained from the Einstein relation shown in Table 1.1, with the corresponding timescale given by $\tau_{diff} = \Lambda^2/2D$, where Λ is the characteristic diffusion length and is assumed to be the thickness of the sheath, or the positive column, for this purpose. For ionization, we will represent this by Townsend's first coefficient α to model the timescale for ionization, such that, $\tau_{ion} = 1/(\alpha|\boldsymbol{v_{dr,e}}|)$ where $v_{dr,e}$ is the drift velocity of the electron. The

Townsend ionization coefficient depends on the electric field and will vary significantly between regions. The final timescale represents the recombination of charged particles. This process is governed by recombination frequency, typically represented by β, such that recombination is given by $\tau_{recomb} = 1/\beta n_i$.

Table 1.2 summarizes the timescales for the cathode sheath and the positive column. Timescales are given for ions and electrons. At a sub-atmospheric pressure without including any excited states or electromagnetic fields there are already significant differences between the different processes. The fastest and slowest processes are presented in bold. Ionization in the cathode sheath is the fastest timescale (7.18×10^{-11} s); recombination in the cathode sheath is the slowest timescale (0.5 s).

Table 1.1 Constants used to determine the various plasma timescales for N_2 gas with units in square brackets. Here, k_B is Boltzmann constant, e is the unit electric charge, the pressure p = 60 Torr, the electron temperature T_e = 11,604 K (~1 eV), and the ion temperature T_+ = 300 K. These equations require E in units V/cm.

Variable	**Electron**	**Ion**
Mobility (μ)	$\mu_e = 400 * (760/p)$ [cm^2/V/s]	$\mu_+ = 2.75 * (760/p)$ [cm^2/V/s]
Diffusion coefficient (D)	$\mathrm{D_e} = \mu_e k_B T_e/e$ [cm^2/s]	$D_+ = \mu_+ k_B T_+/e$ [cm^2/s]
Ionization (α)	$\alpha = 12p \exp\left[-\frac{342}{E/p}\right]$ [cm^{-1}]	
Recombination (β)		$\beta = 2.0 \times 10^{-7}$[cm^3/s]

Table 1.2 Timescales for various processes in the cathode sheath and the positive column. The fastest and slowest time scales in the cathode sheath are in **bold**.

Process	Cathode Sheath (s)	Positive Column (s)
Electron Drift	2.63×10^{-9}	1.97×10^{-8}
Ion Drift	3.82×10^{-7}	2.87×10^{-6}
Electron Diffusion	3.94×10^{-8}	6.31×10^{-7}
Ion Diffusion	5.74×10^{-6}	9.19×10^{-5}
Ionization	$\mathbf{7.18 \times 10^{-11}}$	6.47×10^{-8}
Recombination	$\mathbf{0.5}$	8.51×10^{-8}

An ideal code would directly couple a plasma solver (PS) to a flow solver for examining combustion enhancement or aerodynamic control to more completely characterize behavior from the initial dynamics of excited and ionized species to the later shock propagation and wave pattern generation. The timescales over which plasma dynamics dominate differ from those associated with flow dynamics by a few orders of magnitude, as demonstrated qualitatively in Figure 1.7.

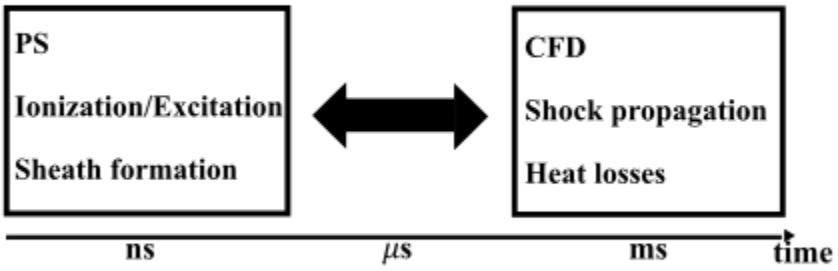

Figure 1.7 Qualitative representation on the timescales between the plasma solver (PS) and computational fluid dynamics (CFD) models

While the physical timescales limit the calculation depending on the region of the column, there are additional numerical timescales that will further limit simulations. A self-consistent solution is achieved by coupling the Lorentz force equation and Maxwell's equations. When the solution is electrostatic, this is achieved by coupling Poisson's equation, $\partial^2\phi/\partial x^2 = (\rho/\epsilon_0)(n_i - n_e)$, where ϕ is the electrostatic potential, ρ is the space charge density, ϵ_0 is the permittivity of free

space, n_e is the electron density, and n_i is the ion density, to the conversation equations. The relative error of this equation will intensify in the positive column where the region is quasi-neutral ($n_i \approx n_e$). Computationally this would require more iterations in this region to reach a convergent solution.

The four important physical timescales discussed have discrepancies between the cathode sheath and the positive column, and for a computational solution there are numerical timescales that can limit the time required to produce a solution. Two key numerical timescales are the Courant-Fredrick-Lewy (CFL) and the dielectric relaxation timescales. The timescales as they relate to the plasma discharge simulations in equation form are described in Section 3.1.1. The CFL condition states the time step of choice must be smaller than the fastest species rate processes occurring within the plasma, (electron velocity and electron diffusion). Specifically, for explicit time stepping, failing to satisfy these conditions leads to an incorrect result. Second is the dielectric relaxation timescale that comes from coupling the governing equations and Poisson's equation. Stiffness between these equations requires a small time-step for numerical stability. Numerical conditions will help choose an appropriate model to simulate the problem of low temperature gas discharge.

1.3.2 Physical Models

Experimental studies on plasma applications show that the technology is feasible and supported by computational models. Any plasma calculation runs the risk of becoming very complicated very quickly depending on the amount of details included. Reducing the computational cost requires making assumptions that may compromise the physics. The goal is to optimize the balance between incorporating the maximum amount of physics within a reasonable computational expense.

The physical description comes from Boltzmann's equation. The equation describes the statistical behavior of particles that are not in equilibrium. When the system is in thermal equilibrium it can readily be solved for several macroscopic parameters. For a nonequilibrium plasma, it becomes difficult to solve the Boltzmann equation for the macroscopic parameters; however, it is still the fundamental approach to describe particle transport. The Boltzmann equation is

$$\frac{\partial f_j}{\partial t} + \vec{v_j} \cdot \nabla f_j - \frac{q\boldsymbol{E}}{m_j} \cdot \nabla_{\mathrm{v}} f_j = C(f_j), \tag{1.6}$$

where f_j is the seven-dimensional distribution of species represented in phase space, velocity space and time, ∇ and ∇_v are the gradient operator in phase space and velocity space, respectively, and $C(f_j)$ is the rate of change of f due to collisions.

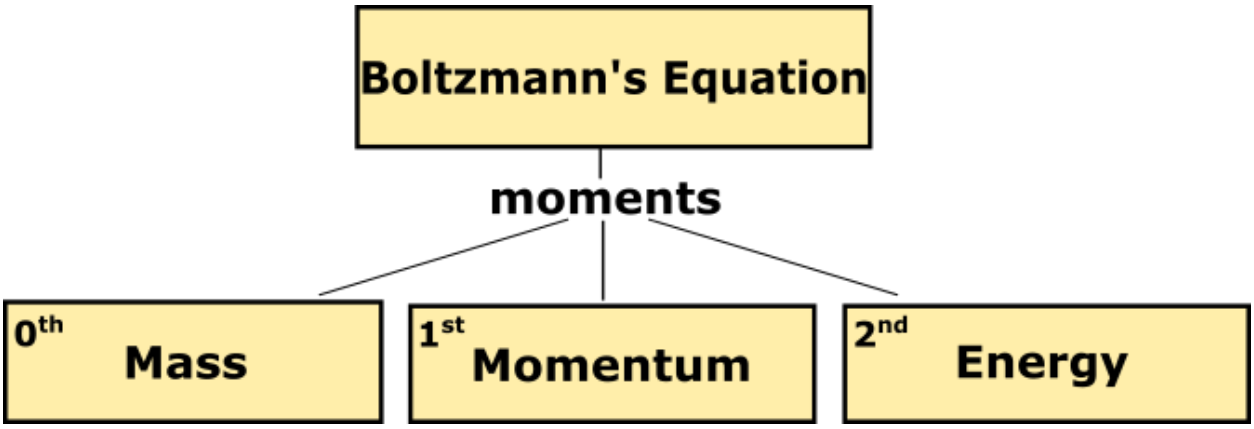

Figure 1.8 Qualitative representation of the process for determining the moments of Boltzmann's transport equation.

The macroscopic variables such as continuity, momentum, and energy can be derived directly from the Boltzmann equation. Figure 1.8 qualitatively shows how the macroscopic parameters are derived by taking moments of the transport equation. When modeling, each species is represented by a transport equation. The accuracy of the model comes from the number of moments and species that are being considered; however, this can increase computational time exponentially. Reducing the number of moments and considering fewer species facilitates the computation, and models often compromise between the moments considered and species considered. Numerical models commonly use either the kinetic description, the fluid description, or a combination of the two. The next section discusses the simplifications necessary for each approach and considerations for selecting the appropriate approach for a given problem.

1.3.3 Kinetic vs. Continuum approach

Starting from the fundamental description of particle motion from Boltzmann's equation, we can derive various sets of transport equations based on different initial assumptions. Each model makes different simplifications, which have associated complications. Numerical models primarily use either the kinetic or fluid approach with hybrid methods combining aspects of these approaches.

The kinetic approach describes the plasma species by a distribution in time and space with each particle defined by a velocity and position at a point in the distribution. Only considering the *x*-direction from the six-dimensional phase space facilitates the integration of Boltzmann's equation for the model. Hitchon developed a direct integration technique that used propagators to evaluate the time evolution of the distribution function [57]. Hitchon's solution separated pure ballistic movement from scattering and then combined the two movements to find the new microscopic values at the new time step [57]. This method remains challenging and requires making significant simplifications to the scattering term. Early kinetic methods were the particle-in-cell (PIC) and Monte Carlo collision (MCC) methods; over the years, a hybrid of the two, PIC/MCC, has become the most popular [58,59].

Without making large simplifications, PIC tracks charged particles within a given frame, while calculating continuity and momentum simultaneously based on how the electric or magnetic field is influencing the movement. This method is consistent in retaining nonlinear effects, space charge and other collective behavior when coupling the equation for charged particle motion with Maxwell's equations [58]. MCC uses species populations represented by particles in time and space to model the production and loss terms stochastically [60]. This method relies on energy dependent cross-sections to predict electron-neutral, ion-neutral collisions. Physical accuracy requires tracking a large number of particles. When combining PIC/MCC methods, the ions and electrons are tracked using PIC and the collisions are determined with MCC. One dimensional PIC/MCC methods have been useful in studying low pressure discharges and microdischarges[19,61–63].

The challenges of kinetic modeling are in the computational efficiency with large systems for time and space scales. Kinetic methods will not be suited for a high collisional environment at atmospheric pressure [19]. Moreover, PIC/MCC may encounter difficulties in resolving the edge of

the distribution and processing large amounts of data. Managing large amounts of data often requires using averaged raw population data as a function of position. Although computers have increased in storage capacity, this approach still facilitates since current hardware still has limitations.

The kinetic approach provides a detailed description of the plasma. Simplicity and ease of computation motivate the application of a continuum or fluid model. The fluid model describes the plasma more collectively [60]. Averaged values of the density, mean velocity, and mean energy are taken as moments of the Boltzmann distribution [6]. This differs from the kinetic method in that it uses a more collective technique rather than describing the plasma with its individual properties. The most common characterization method separates the ions and electrons to solve for the macroscopic quantities.

Fluid models are adequate when the collision frequency is high. Parameters that affect the reliability of using a fluid model are the pressure and the ratio of the mean free path to the characteristic length. Adapting the conservation equations (1.3)-(1.5) for a plasma fluid for each species yields

$$\frac{\partial \rho_{m_j}}{\partial t} + \nabla \cdot (\rho_{m_j} \vec{u}_j) = C_j \tag{1.7}$$

$$\frac{\partial \rho_{m_j} \vec{u}_j}{\partial t} + \nabla \cdot \left(\rho_{m_j} \vec{u}_j \vec{u}_j\right) = -\nabla p_j + \rho_j \vec{E} - \rho_{m_j} \vec{g} \tag{1.8}$$

and

$$\frac{\partial}{\partial t}\left(\frac{\rho_{m_j} u^2}{2} + \frac{3}{2} p_j\right) + \nabla \cdot \left[\left(\frac{\rho_{m_j} u^2}{2} + \frac{3}{2} p_j\right) \vec{u}_j\right] = -\nabla \cdot \vec{q}_j - \left(\vec{u}_j \cdot \nabla p_j\right) + \rho_j \vec{u}_j \cdot \vec{E} + \rho_{m_j} \vec{u}_j \cdot \vec{g} \tag{1.9}$$

where, ρ_{m_j} is the mass density, and ρ is the space charge density, q is the heat flux, and C is the source term of collisions for species j. Equations (1.7)-(1.9) are the first three moments of Boltzmann's equation. Simulations involving these full equations with detailed chemistry are

computationally costly, motivating the following simplifications to make computational time more manageable.

Simplifying the momentum equation reduces the number of moments being solved. Neglecting the inertia of the charged particles so that the mean velocities respond to changes in the electric field gives the DD approximation, which only includes the drift and diffusion components. The DD approximation is also known as the one-moment model. This approximation works if the acceleration of the species is much smaller than the magnitude of the elastic collisions and the force of the electric field. Generally, if the pressure is above 100 mTorr then the DD approximation is valid, otherwise the full momentum equation should be used [64]. The one moment model consists of the continuity equation, given by

$$\frac{\partial n_j}{\partial t} + \frac{\partial \mathbf{\Gamma}_j}{\partial x} = C_j \tag{1.10}$$

and Poisson's equation, given by

$$\frac{\partial^2 \phi}{\partial x^2} = -\frac{\rho}{\epsilon_0}, \tag{1.11}$$

where n is the concentration of species, Γ is the movement or flux of the species (comprised of drift and diffusion components), and C_j is the collision term of species j. Chapter 2 discusses the numerical methods for solving (1.10)-(1.11).

The accuracy of this model depends critically on the quality of the approximation for the collision term. While the Townsend ionization model often works, it remains inconsistent in different regions. One common assumption is that the electrons are in equilibrium with the electric field; however, this is no longer valid in areas with more space charge [14]. In the positive column, where the electric field remains approximately constant with position, the model accurately captures species production. However, in the cathode region, where there is a buildup of space charge and the electric field varies rapidly, the Townsend ionization model agrees poorly. One may also use correlations from chemical rate equations to describe species production [65–67]. Both methods have advantages and disadvantages and will be discussed in the methods section.

As a first step to understanding behavior of NPPs, this thesis develops a fluid-based simulation to analyze plasma species generation for different EP parameters, specifically electric field intensity and pulse duration for two gases (argon and air) at two pressures. Chapter 2 outlines the methods used for developing the one moment model. Chapter 3 applies this model to single and multiple pulses applied to either air or argon and investigates the impact of changing pulse conditions on species. Concluding remarks and outline potential future simulations and experiments are provided in Chapter 4.

2. METHODS

The fundamentals of gas discharges presented in the previous chapter lay the groundwork for the physics that take place when creating a plasma and tackling the challenges associated with a problem solved numerically. Experiments have shown plasma technology can support applications in several disciplines, but much can still be gained from modeling the chemistry and dynamics. This chapter details the governing equations for the model, the discretization methods used, and the chemistry models of choice.

2.1 Model

As previously discussed, this analysis considers the one-moment or DD model. For a plate-to-plate nanosecond EP, the model was developed to represent the storage of energy in excited molecular states and subsequent correlations of PGRS through altering pulse parameters. The species motion is described by the DD approximation [46] and employs a numerical finite difference scheme coupled to Poisson's equation in a time marching scheme. The simulation considers the one-dimensional planar geometry shown in Fig. 2.1 with a gap distance of 2 cm and initial electric field of zero. The right electrode was grounded and the applied EP at the left electrode was assumed as Gaussian with respect to time as

$$V_{applied} = -V_p \exp\left[\left(\frac{t - t_p}{\sigma}\right)^2\right], \tag{2.1}$$

where we nominally set V_p = 850 V, t_p = 78.5 ns, and σ = 3 ns. This geometry differs from [46] by placing the electrodes in direct contact with the fill gas rather than separating them with a dielectric interface.

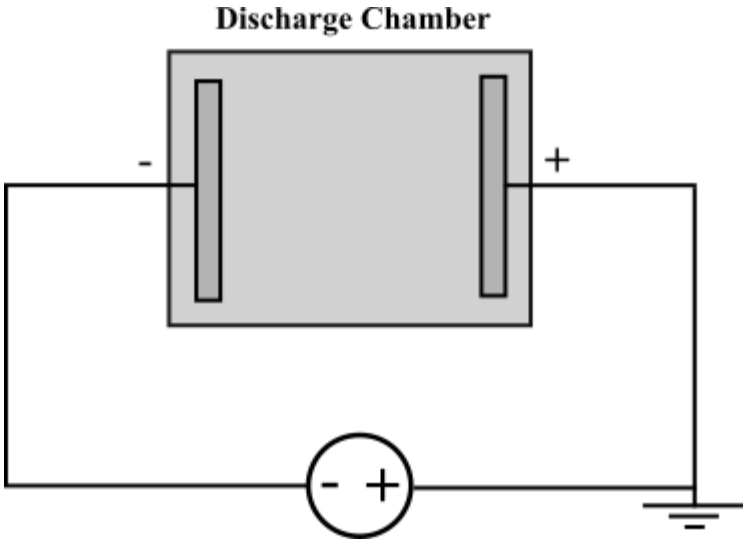

Figure 2.1 Geometry for gas discharge.

The plasma is formed between the plates in the discharge chamber when the applied pulse is introduced. To begin, we also want to state the assumptions that are made for this problem. The assumptions are listed below:

1. The state of the neutral gas in the discharge chamber is considered constant. The motion of the neutral particles is neglected.
2. The ions and neutral species are in thermal equilibrium. The temperature will remain temporally and spatially uniform.
3. Low pressures are studied and assumed continuum approaches are considered valid.
4. There is no magnetic field present, and no magnetohydrodynamics are considered.
5. Negative ions are not considered.

Stating these assumptions lays the groundwork for the form of the equations representing the plasma discharge, discussed next.

2.2 Governing Equations

Inside the domain, continuity equations were solved for the number density of each species. We coupled the continuity of each species *j*, given by

$$\frac{\partial n_j}{\partial t} + \frac{\partial \mathbf{\Gamma}_j}{\partial x} = C_j, \tag{2.2}$$

where n is the concentration of species, Γ is the flux of the species, and C_j is the collision terms, with Poisson's equation, given by

$$\frac{\partial^2 \phi}{\partial x^2} = -\frac{\rho}{\epsilon_0}, \tag{2.3}$$

where ϕ is the electric potential, ρ is the space charge, and ϵ_0 is the permittivity of free space. The flux for each species Γ_j is

$$\mathbf{\Gamma}_j = s_j \mu_j n_j \boldsymbol{E} - D_j \left(\frac{\partial n_j}{\partial x} \right), \tag{2.4}$$

where the first term on the right-hand side (RHS) represents drift and the second term represents diffusion. The drift term consists of s_j, the sign of the charged species j (+1 for positive charged species and -1 for electrons), μ_j is the mobility of species j, n_j is the number density of species j, and E is the electric field. The diffusion component consists of the first derivative of the number density with respect to space and the diffusion coefficient of the species j. Again, we restate that negative ions are not being considered in this study.

We obtain C_j, from (2.2) by finite rate chemistry as

$$\sum_{j=1}^{B} v_{rj} M_j \rightarrow \sum_{j=1}^{B} v'_{rj} M_j \tag{2.5}$$

$$C_j = \sum_{r}^{A} \left(v'_{rj} - v_{rj} \right) k_r \prod_{t=1}^{B} n_t^{v'_{rt}}, \tag{2.6}$$

where v_{rj}, and v'_{rj} are the stoichiometric coefficients for the reactants and products for species j in reaction r, M_j is the chemical symbol for species j, A is the total number of reactions, B is the total number of species, and k_r, is the rate coefficient for each reaction mechanism.

2.3 Numerical Discretization

For this one-dimensional problem, the limitations come from having vastly different time scales like ionization, recombination, drift, and diffusion, as previously discussed. The stiffness from these terms leads to computational difficulties. A combination of numerical techniques can be used help to combat the stiffness. For this model, we combine a central finite-difference scheme with the Scharfetter-Gummel scheme, which is an exponential discretization that provides a self-consistent solution between the drift and diffusion terms, to treat particle transport. This is possible because we treat the terms other than number density as constant within the computational cell. Discretizing (2.2) by finite difference yields

$$\frac{n_{i,j}^{t+1} - n_{i,,j}^{t}}{\Delta t} + \frac{\boldsymbol{\Gamma}_{i+\frac{1}{2},j}^{t+1} - \boldsymbol{\Gamma}_{i-\frac{1}{2},j}^{t+1}}{\Delta \mathrm{x}} = C_{i,j}^{t}, \tag{2.7}$$

where the flux terms are evaluated on the cell interface and described by the Scharfetter-Gummel scheme as

$$\boldsymbol{\Gamma}_{i+1/2,j} = -\frac{s_j}{\Delta x} u_{i+\frac{1}{2},j} (\phi_{i+1} - \phi_i) \left[\frac{n_{i+1,j}}{1 - \exp\left(z_{i+\frac{1}{2},j}\right)} + \frac{n_{i,j}}{1 - \exp\left(-z_{i+\frac{1}{2},j}\right)} \right], \tag{2.8}$$

where

$$z_{i+\frac{1}{2},j} = -s_j \frac{\mu_{i+\frac{1}{2},j}}{D_{i+\frac{1}{2},j}} (\phi_{i+1} + \phi_i). \tag{2.9}$$

For the limiting cases, such as assuming predominantly movement from diffusion, the scheme becomes centrally differenced. For strong electric fields, where there is predominantly movement from drift, the scheme becomes a first order upwind difference.

Treating Poisson's equation explicitly assumes a constant electric field between time steps; however, the electric field is not constant in space. Also, the strong coupling between charged

particles and the electric field restricts the time step significantly to achieve this explicitly. In order to achieve a solution, the defined time step must be shorter than the dielectric relaxation time. Dielectric relaxation time can be found by dividing the permittivity of free space by the plasma conductivity. For a high density, low pressure discharge, Ventzek[68] calculated , the dielectric relaxation time $\Delta t_{diel} \approx 10^{-13}$–$10^{-12}$ s. We keep the time step small for treating the transport equation to satisfy the limiting dielectric relaxation time step. Solving Poisson's equation will require an explicit approach whether the charge densities are determined implicitly or explicitly. The difference scheme solves for the new value of the potential at the new time step based on the charge densities that were found at the new time step. Thus, we may write (2.3) as

$$\frac{\phi_{i+1} - 2\phi_i + \phi_{i-1}}{\Delta x^2} = -\frac{\sum_{j=0} q_j n_{i,j}}{\epsilon_0} \tag{2.10}$$

or

$$\phi_{i+1} - 2\phi_i + \phi_{i-1} = -\frac{\sum_{j=0} q_j n_{i,j}}{\epsilon_0} \Delta x^2, \tag{2.11}$$

where q_j is the charge of species j. We solve (2.11) by writing it in matrix form, such that $Ax = b$, where A is the coefficient tridiagonal matrix for the left-hand side (LHS), x is solved for new values of the potential across the grid, and b represents the RHS, comprised of the number densities at the current time step.

2.4 Boundary Conditions

Boundary conditions with a constant temperature along the electrode were used for neutral particles. The number density of the bulk gas was set to an initial value based on the pressure (3 Torr) and determined by the ideal gas law such that $n_{bulk} = p/(k_b T_{bulk})$. This is a weakly ionized plasma where we initially set the ionization fraction of the ions and electrons to $n_+ = n_e = n_{bulk} \times 10^{-8}$, which provides a sufficiently high ratio for a convergent solution. We applied the following simplified boundary conditions in Table 2.1 for the charged particles. [69]

Table 2.1 Boundary conditions for gas discharge

Cathode ($x = 0$)	**Anode ($x = d$)**
$\Gamma_e = \gamma\Gamma_+$	$\Gamma_+ = 0$
$\frac{\partial n_+}{\partial x} = 0$	$\frac{\partial n_e}{\partial x} = 0$
$\phi(0) = V_{app}$	$\phi(d) = 0$

First, the general mechanism for electron emission at the cathode wall was determined by secondary electron emission. For nitrogen, values of secondary emission range from, $10^{-1} > \gamma > 10^{-2}$ [69]. Additionally, we set the normal derivative of the ion density to zero. Then, assuming the anode reflects all ions, then flux at the anode is zero. Furthermore, we set the normal derivative of the electron density to zero on the anode boundary. The potential was specified as the applied voltage at the cathode and grounded at the anode.

Additionally, the total current is calculated at the powered electrode, and for present calculations is the cathode. For a gas discharge the total current is the sum of the conduction current and the displacement current. Conduction current is calculated as the sum of flux times species charge and displacement current is obtained from the rate of change of the electric field over the gap. The sum may be written as

$$I = -\iint \vec{J_t} \cdot \hat{n} dA = -\iint \left[\left(\sum_j q_j \Gamma_j \right) + \epsilon_0 \frac{\partial E}{\partial t} \right] dA, \tag{2.12}$$

where J_t is the total current density, $\hat{n}$ is the vector normal to the computational domain, and A is the area. For completeness the charge conservation equation is

$$\nabla \vec{J_c} + \frac{\partial \rho}{\partial t} = 0. \tag{2.13}$$

Large contributions of current can be seen from including the displacement current for an unsteady problem. Displacement current often dominates, and therefore is included in this analysis. The displacement current is represented by

$$\overrightarrow{J_d} = \epsilon_0 \frac{\partial \vec{E}}{\partial t}, \tag{2.14}$$

where the displacement current is discretized with second order accuracy by storing values of the electric field from previous time steps.

2.5 Gas Properties

This study considers argon and air as the fill gases. The gas is assumed to be weakly ionized such that most of the collisions will occur with neutral particles. A five-species model with argon as the bulk gas was first employed for basic understanding of model development. For argon chemistry this model specifically considered five species: electrons (e), two ions ($Ar^+$and Ar_2^+), an excited state (Ar*), and a neutral state (Ar). The charged particle properties were based on those employed in [70]. The mobility of particles in the gas phase is $\mu_j = e/m_j \nu_m$, where, e is the elementary charge, m is the mass of the species j, and ν_m is the momentum transfer collision frequency. Diffusion of species j is determined from the Einstein relation $D_j = k_B T_j / m_j \nu_m = \mu_j k_B T_j / e$, where k_B is Boltzmann's constant and T_j is the temperature of each species j. Table 2.2 summarizes the ion and electron mobilities and diffusion coefficients for argon.

Table 2.2 Transport coefficients for argon. Here, p is in Torr and E is in V/cm.

Species	**Mobility [cm^2 V^{-1} s^{-1}]**	**Diffusion Coefficient [cm^2/s]**	**Ref**
e	BOLSIG+	BOLSIG+	[71]
Ar^+	$10^{-1} \times \frac{1 - 2.22 \times 10^{-3}(E/p)}{P}$ $\quad \frac{E}{p} \leq 60 \left[\frac{\text{V}}{\text{cm} \cdot \text{Torr}}\right]$ $\frac{8.25 \times 10^3}{p\sqrt{E/p}}\left(1 - \frac{86.52}{(E/p)^{3/2}}\right)$ $\quad \frac{E}{p} > 60 \left[\frac{\text{V}}{\text{cm} \cdot \text{Torr}}\right]$	Einstein Relation	[72]
Ar_2^+	$1.83 \times 10^{-4}\left(\frac{760}{p}\right)$	Einstein Relation	[70]
Ar^*	$\emptyset$	$2.42 \times 10^{19}/n_{bulk}$	[14,73]

The electron transport properties are found by solving the EEDF function using the well know Boltzmann solver, BOLSIG+. The secondary emission coefficient was fixed at $\gamma = 0.1$. We used a two-temperature model such that the ion temperature represents the bulk, and the electron temperature is given by $T_e = f(E/N)$ obtained from BOLSIG+ [71].

Next, we considered air chemistry with $\gamma = 0.1$. We consider 23 species, electrons, three ions, six neutrals, five excited states and eight vibrational states. Table 2.3 summarizes the ion and electron mobilities and diffusion coefficients for air.

Table 2.3 Transport coefficients for air with n_{bulk} in m^{-3}

Species	Mobility [$m^2V^{-1}s^{-1}$]	Diffusion Coefficient [m^2/s]	Ref
e	BOLSIG+	BOLSIG+	[71]
N_2^+	$5.4 \times 10^{21}/n_{bulk}$	Einstein Relation	[74]
O_2^+	$6.4 \times 10^{21}/n_{bulk}$	Einstein Relation	[74]
O^+	$8.0 \times 10^{21}/n_{bulk}$	Einstein Relation	[75]
N_2	$\emptyset$	$4.9 \times 10^{20}/n_{bulk}$	[76]
O_2	$\emptyset$	$4.9 \times 10^{20}/n_{bulk}$	[76]
N	$\emptyset$	$6.8 \times 10^{20}/n_{bulk}$	[77]
O	$\emptyset$	$7.8 \times 10^{20}/n_{bulk}$	[78]
NO	$\emptyset$	$6.2 \times 10^{20}/n_{bulk}$	[76]
O_3	$\emptyset$	$3.1 \times 10^{20}/n_{bulk}$	[79]
$N_2(A^3\Sigma)$	$\emptyset$	$4.9 \times 10^{20}/n_{bulk}$	[76]
$N_2(B^3\Pi)$	$\emptyset$	$4.9 \times 10^{20}/n_{bulk}$	[76]
$N_2(C^3\Pi)$	$\emptyset$	$4.9 \times 10^{20}/n_{bulk}$	[76]
$N_2(a'^1\Sigma)$	$\emptyset$	$4.9 \times 10^{20}/n_{bulk}$	[76]
$O(^1D)$	$\emptyset$	$7.8 \times 10^{20}/n_{bulk}$	[78]
$N_2(v = 1 - 8)$	$\emptyset$	$4.9 \times 10^{20}/n_{bulk}$	[76]

The robustness of the model comes from the descriptions of the reaction mechanisms and the reaction rates that are used. The reaction mechanisms for argon includes electron-impact ionization, ground-state excitation, stepwise ionization, atomic de-excitation, dissociative recombination, atomic excitation, three body recombination, atomic molecular ion conversion, and metastable associative ionization. Table 2.4 summarizes the reaction rates used for argon.

Table 2.4 Reaction mechanism and rates for argon. The units for number densities are in m^{-3} and electron temperature T_e are in eV. Reaction rates are consistent with one-body rates in s^{-1}, two-body rates in $m^3\ s^{-1}$, and three-body rates in $m^6\ s^{-1}$.

No.	Reaction	Rate	Ref
(1)	$e + Ar \rightarrow Ar^+ + 2e$	$k = 4.0 \times 10^{-18} T_e^{0.5} \exp[-15.8/T_e]$	70,71
(2)	$e + Ar \rightarrow Ar^* + e$	$k = 1.0 \times 10^{-17} T_e^{0.75} \exp[-11.6/T_e]$	70,71
(3)	$e + Ar^* \rightarrow Ar^+ + 2e$	$k = 1.0 \times 10^{-16} T_e^{3} \exp[-4.16/T_e]$	70,71
(4)	$e + Ar^* \rightarrow Ar + e$	$k = 1.0 \times 10^{-17} T_e^{0.75}$	70,71
(5)	$e + Ar_2^+ \rightarrow Ar^* + Ar$	$k = 5.38 \times 10^{-14} T_e^{-0.66}$	70
(6)	$e + Ar^+ \rightarrow Ar^*$	$k = 4.00 \times 10^{-19} T_e^{-0.5}$	70
(7)	$e + e + Ar^+ \rightarrow Ar^* + e$	$k = 5.00 \times 10^{-33} T_e^{-4.5}$	70
(8)	$Ar^+ + 2Ar \rightarrow Ar_2^+ + Ar$	$k = 2.50 \times 10^{-37}$	70
(9)	$Ar^+ + Ar^* \rightarrow Ar^+ + Ar + e$	$k = 5.0 \times 10^{-16}$	70

Similarly, but with more detail, the reaction mechanisms for air includes electron-impact reactions (reactions (1)–(10) and (43)–(50)), reactions with neutral radicals (reactions (11)–(17)), quenching and other transitions (reactions (18)–(32)), charge-exchange reactions (reactions (33) and (34)), and electron–ion recombination (reactions (35)–(42)). Table 2.5 and Figure 2.2 provide the rate coefficients [65].

Table 2.5 Reaction mechanism and rates for air. The units for number densities are in cm^{-3}, and both the gas temperature T and electron temperature T_e are in K. Reaction rate units are consistent with one-body rates in s^{-1}, two-body rates in $cm^3\ s^{-1}$, and three-body rates in $cm^6\ s^{-1}$.

No.	Reaction	Rate	Ref
(1)	$e + N_2 \rightarrow N_2^+ + 2e$	Figure 2.2a	[65]
(2)	$e + O_2 \rightarrow O_2^+ + 2e$	Figure 2.2a	[65]
(3)	$e + O_2 \rightarrow O + O^+ + 2e$	Figure 2.2a	[65]
(4)	$e + N_2 \rightarrow N_2(A^3\Sigma) + e$	Figure 2.2a	[65]
(5)	$e + N_2 \rightarrow N_2(B^3\Pi) + e$	Figure 2.2a	[65]
(6)	$e + N_2 \rightarrow N_2(C^3\Pi) + e$	Figure 2.2a	[65]
(7)	$e + N_2 \rightarrow N_2(a'^1\Sigma) + e$	Figure 2.2a	[65]
(8)	$e + N_2 \rightarrow N + N + e$	Figure 2.2a	[65]
(9)	$e + O_2 \rightarrow O + O + e$	Figure 2.2a	[65]
(10)	$e + O_2 \rightarrow O + O(^1D) + e$	Figure 2.2a	[65]
(11)	$N + O_2 \rightarrow NO + O$	$k = 1.1 \times 10^{-14} T \exp[-3150/T]$	[65]
(12)	$N + NO \rightarrow N_2 + O$	$k = 1.1 \times 10^{-12} T^{0.5}$	[65]
(13)	$O + O_3 \rightarrow O_2 + O_2$	$k = 2.0 \times 10^{-11} \exp[-2300/T]$	[65]
(14)	$O + O + N_2 \rightarrow O_2 + N_2$	$k = 2.8 \times 10^{-34} \exp[720/T]$	[65]
(15)	$O + O + O_2 \rightarrow O_2 + O_2$	$k = 2.5 \times 10^{-31} T^{-0.63}$	[65]
(16)	$O + O_2 + N \rightarrow O_3 + N_2$	$k = 5.6 \times 10^{-29} T^{-2.0}$	[65]
(17)	$O + O_2 + O_2 \rightarrow O_3 + O_2$	$k = 8.6 \times 10^{-31} T^{-1.25}$	[65]
(18)	$N_2(A^3\Sigma) + O_2 \rightarrow N + O + O$	$k = 1.7 \times 10^{-12}$	[65]
(19)	$N_2(A^3\Sigma) + O_2 \rightarrow +N_2 + O_2$	$k = 7.5 \times 10^{-13}$	[65]
(20)	$N_2(A^3\Sigma) + O \rightarrow N_2 + O(^1D)$	$k = 3.0 \times 10^{-11}$	[65]
(21)	$N_2(A^3\Sigma) + N_2(A^3\Sigma) \rightarrow N_2 + N_2(B^3\Pi)$	$k = 7.7 \times 10^{-11}$	[65]
(22)	$N_2(A^3\Sigma) + N_2(A^3\Sigma) \rightarrow N_2 + N_2(C^3\Pi)$	$k = 1.6 \times 10^{-10}$	[65]
(23)	$N_2(B^3\Pi) + N_2 \rightarrow N_2(A^3\Sigma) + N_2$	$k = 3.0 \times 10^{-11}$	[65]
(24)	$N_2(B^3\Pi) \rightarrow N_2(A^3\Sigma) + h\nu$	$k = 1.5 \times 10^{5}$	[65]

Table 2.5 continued

(25)	$N_2(B^3\Pi) + O_2 \rightarrow N_2 + O + O$	$k = 3.0 \times 10^{-10}$	[65]
(26)	$N_2(a'^1\Sigma) + N_2 \rightarrow N_2 + N_2$	$k = 2.0 \times 10^{-13}$	[65]
(27)	$N_2(a'^1\Sigma) + O_2 \rightarrow N_2 + O + O(^1D)$	$k = 2.8 \times 10^{-11}$	[65]
(28)	$N_2(C^3\Pi) + N_2 \rightarrow N_2(B^3\Pi) + N_2$	$k = 1.0 \times 10^{-11}$	[65]
(29)	$N_2(C^3\Pi) \rightarrow N_2(B^3\Pi) + hv$	$k = 3.0 \times 10^{7}$	[65]
(30)	$N_2(C^3\Pi) + O_2 \rightarrow N_2(A^3\Sigma) + O + O$	$k = 3.0 \times 10^{-10}$	[65]
(31)	$O(^1D) + N_2 \rightarrow +O + N_2$	$k = 2.6 \times 10^{-11}$	[65]
(32)	$O(^1D) + O_2 \rightarrow O + O_2$	$k = 4.0 \times 10^{-11}$	[65]
(33)	$O^+ + O_2 \rightarrow O_2^+ + O$	$k = 2.0 \times 10^{-11}$	[65]
(34)	$N_2^+ + O_2 \rightarrow N_2 + O_2^+$	$k = 6.0 \times 10^{-11}$	[65]
(35)	$e + N_2^+ \rightarrow N + N$	$k = 8.3 \times 10^{-6} T_e^{-0.5}$	[65]
(36)	$e + O_2^+ \rightarrow O + O$	$k = 6.0 \times 10^{-5} T_e^{-1.0}$	[65]
(37)	$e + e + N_2^+ \rightarrow N_2 + e$	$k = 1.4 \times 10^{-8} T_e^{-4.5}$	[65]
(38)	$e + e + O_2^+ \rightarrow O_2 + e$	$k = 1.4 \times 10^{-8} T_e^{-4.5}$	[65]
(39)	$e + e + O^+ \rightarrow O + e$	$k = 1.4 \times 10^{-8} T_e^{-4.5}$	[65]
(40)	$e + N_2^+ + M \rightarrow N_2 + M$	$k = 3.1 \times 10^{-23} T_e^{-1.5}$	[65]
(41)	$e + O_2^+ + M \rightarrow O_2 + M$	$k = 3.1 \times 10^{-23} T_e^{-1.5}$	[65]
(42)	$e + O^+ + M \rightarrow O + M$	$k = 3.1 \times 10^{-23} T_e^{-1.5}$	[65]
(43-50)	$e + N_2(v = 0) \rightarrow N_2(v = 1 - 8) + e$	Figure 2.2b	[65]

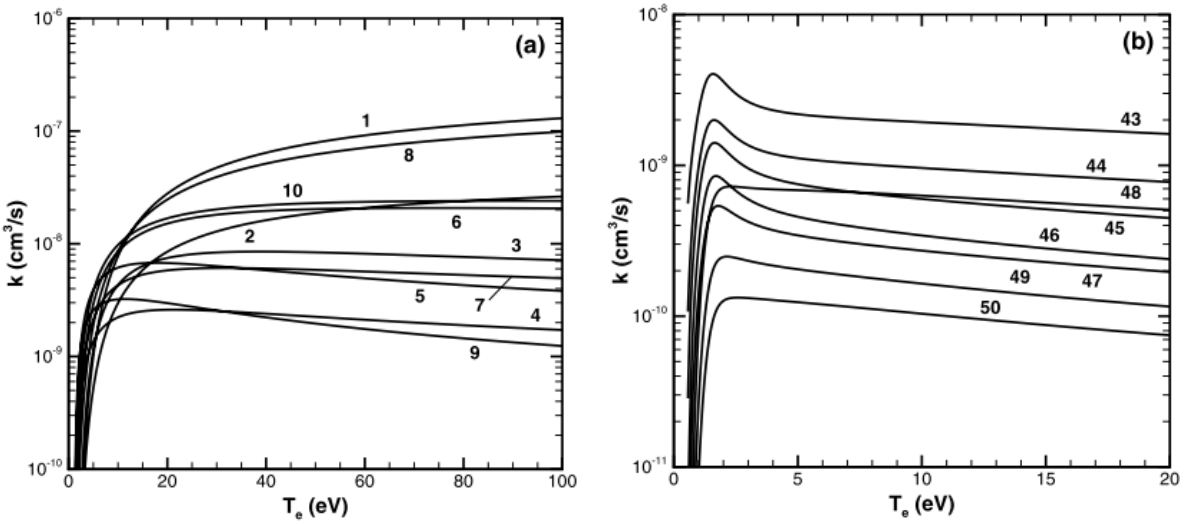

Figure 2.2(a) Ionization and electronic excitation rates for air (reactions (1)–(10) of Table 2.5 [65]). (b) Vibrational excitation rate for air (reactions (43)–(50) of Table 2.5 [65]).

The gas properties are the best current approximations from [65,70]. The two models are tested with these chemistry models and the DD approximation for a variety of EP parameters. It should be noted that the utility of the air model does not perform as well with the DD approximation as compared the five moment model used by Poggie et al. [65], but we use the DD approximation for basic understanding of pulsed power with NPP.

3. SIMULATIONS OF NPP DISCHARGES

The one-moment model that is described in the previous chapter is employed here. This chapter first benchmarks the one moment model described above against a previous simulation [70] and an experiment [80]. The major focuses of this chapter are on the effects of pulse parameters for single and multiple pulsed nanosecond discharges, which is critical for experimental design and utility. Third, we present the results for a case representative of a typical experiment[80] before analyzing the implications of various applied voltages, pulse widths, repetition rates, pulse frequencies, pressures, and gap distances.

3.1 Single Pulse Simulations

The success of these applications depend on plasma generation and the power input to generate these plasma. From a budget perspective the lower amount power that is used to generate the same outcome is generally understood as better. This section studies the applied pulse delivered from a single pulse to the output of the electron and ion densities. Given that this is a computational study we first test the accuacry of the numerical methods by preforming convergence tests. Second, we gain a basic understanding of the EP paramters and their effects. Third, we simulate an experiment done by Paschen to understand scaling of pressure and distance within our problem, ultimatley to understand the scaling of a Gaussian represented NPP.

3.1.1 Resolution

For computational accuracy we test the numerical resolution of the pulse. The length scale is determined by the number of cells divided by the gap distance. The number of cells across the domain is vaired from 100 to 600 cells. Figure 3.1(a) is the result for the single pulse of the argon model taken at the peak voltage. Figure 3.1(b) is the result from a single pulse of the air model taken at the peak voltage. Spatial convergence is achieved for a grid spacing of 5.0×10^{-4} m, or 400 points across the domain.

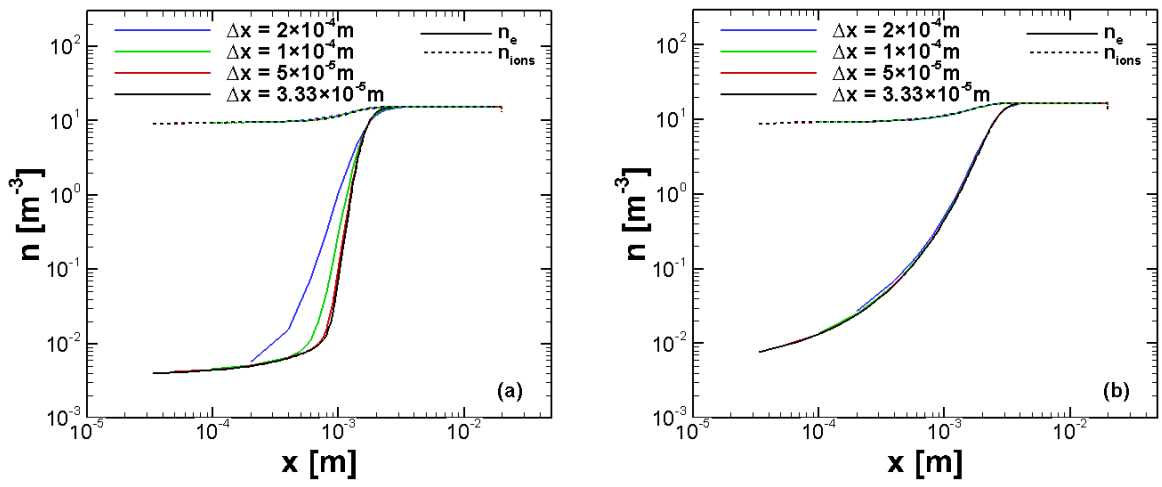

Figure 3.1 Spatial profile for electron (n_e) and ion (n_{ions}) number densities with various grid spacings across the domain taken at the peak voltage (78.5 ns) for (a) argon and (b) air.

Next is the temporal convergence is checked, in which the minimum time step is needed to produce a convergent solution. Figure 3.2(a) is the result for the single pulse of the argon model taken after the period has finished (t =150 ns). Similarly, Figure 3.2(b) is the result from a single pulse of the air model. By varying the time step, Δt, it is shown that a time step of 1.0×10^{-11}s is convergent for the argon model while convergence in the air model is achieved at Δt =5.0×10^{-13} s. It is important to keep in mind the limiting numerical time steps are the CFL and dielectric relaxation time steps. A time step that is larger than the CFL condition will cause the code to crash.

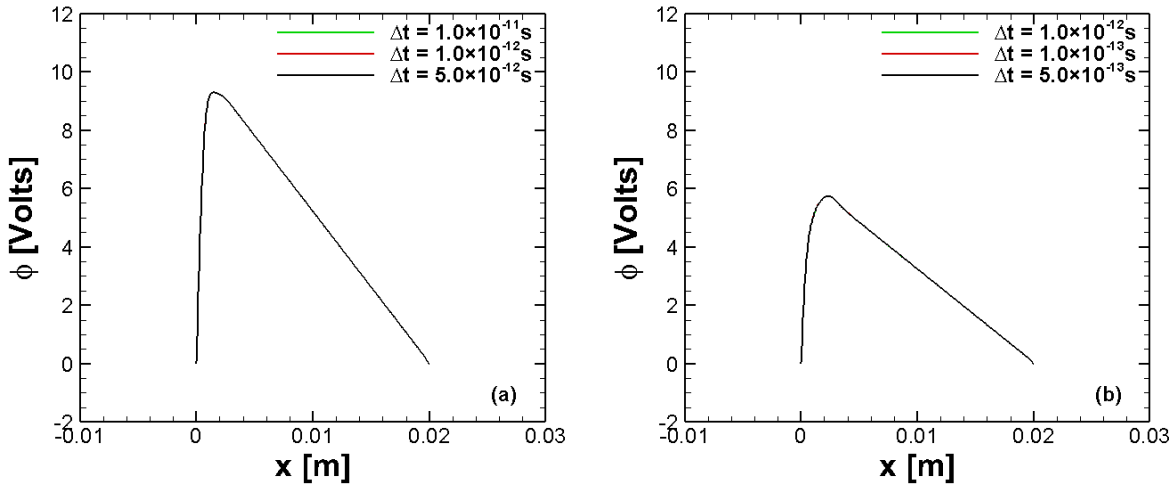

Figure 3.2 Spatial profile for potential ϕ given by varying different time steps across the domain after the pulse (150 ns) for (a) argon and (b) air.

Simulations are also performed with a constant time step and a variable time step. A variable time step was implemented to test a constant time step against the limiting numerical timescales generated from explicit time stepping. Here we test the minimum of four different time steps against a constant time step. A convergent solution must resolve the minimum processes produced by each equation. The equations are as follows: electron diffusion, CFL, dielectric relaxation and the ionization rate.

$$\Delta t_{diff} = \frac{(\Delta x)^2}{D_e} \tag{3.1}$$

$$\Delta t_{CFL} = \frac{(\Delta x)^2}{2D_e + \mu_e |E| \Delta x} \tag{3.2}$$

$$\Delta t_{diel} = \frac{\varepsilon_0}{q(\mu_i n_i + \mu_e n_e)} \tag{3.3}$$

$$\Delta t_{\nu_i} = \frac{1}{\nu_i} \tag{3.4}$$

The minimum step imposed by these four conditions are used to determine the time step required for convergence. Figure 3.3 shows the single input pulse for a constant time step verses a variable time step. The computational time is not expensive, and this simulation is completed very quickly.

In the case of the single pulse, the constant time-step has a higher potential profile than the variable time-step profile which occurs at a slightly lower potential.

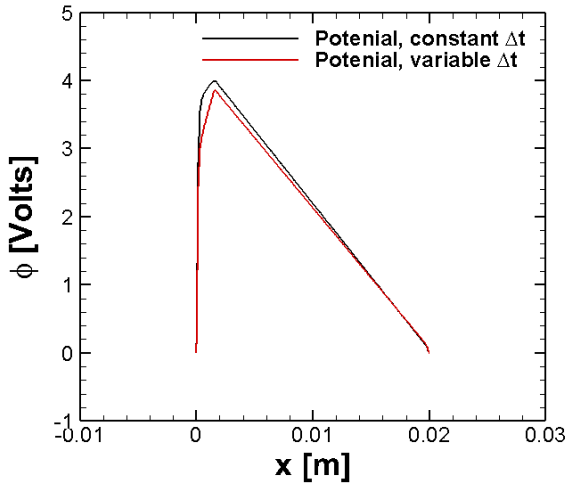

Figure 3.3 Use of a variable timestep represented with potential profile.

3.1.2 Pulse Parameters

Figure 2.1 represents the electrode configuration in a one-dimensional geometry with a 2 cm gap and the background gas of either argon or air. The pressure was fixed at 3 Torr. As a reminder, this section presents the results for a low temperature gas discharge for an experimental applied EP fit by the Gaussian defined in Equation (2.1). with $V_p = 850$ V and $\sigma = 3$ ns. Equation (2.1) was fit with experimental data [80]. The edges of the pulse remain smooth for an easily obtainable numerical solution. Figure 3.4(a) compares the measured applied voltage to the Gaussian fit used in this study. Figure 3.4(b) summarizes our calculation of n_e in argon before the pulse starts (75 ns), at the peak of the pulse (78.5 ns), and after the pulse has decayed (150 ns). During this period, ionization increases over time until sufficient time has passed for ionization to decay, which is beyond the period studied here. Both n_e and n_i increase with time for argon.

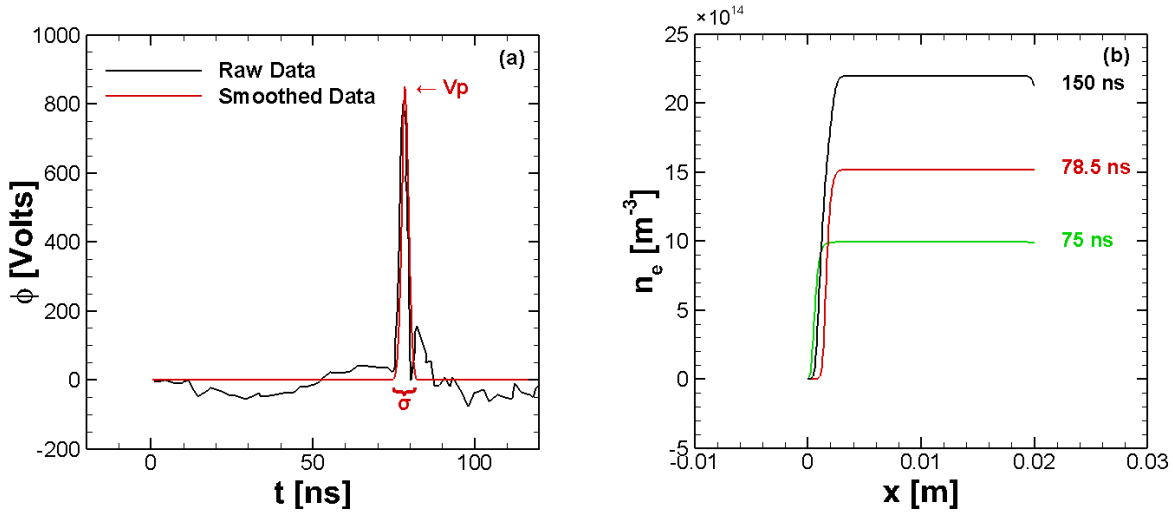

Figure 3.4 Argon model: (a) The applied pulse with a smoothed fit to experimental data; (b) Electron density before the pulse at the peak of the applied pulse, and after the pulse.

We first benchmark this simulation to another simulation that was based on experimental data. Using the applied Gaussian given in Equation (2.1) we compare the result of the nanosecond pulse discharge at the peak of the pulse. Figure 3.5 shows the potential ϕ, electron density n_e, and ion densities n_i, where i=Ar_+, Ar_+^2, for argon. Here, the profiles for the present simulation lack the same spatial curvature as the experimental data due to spatial grid refinement. Better grid resolution should yield a more accurate result with a concomitant increase in computational expense.

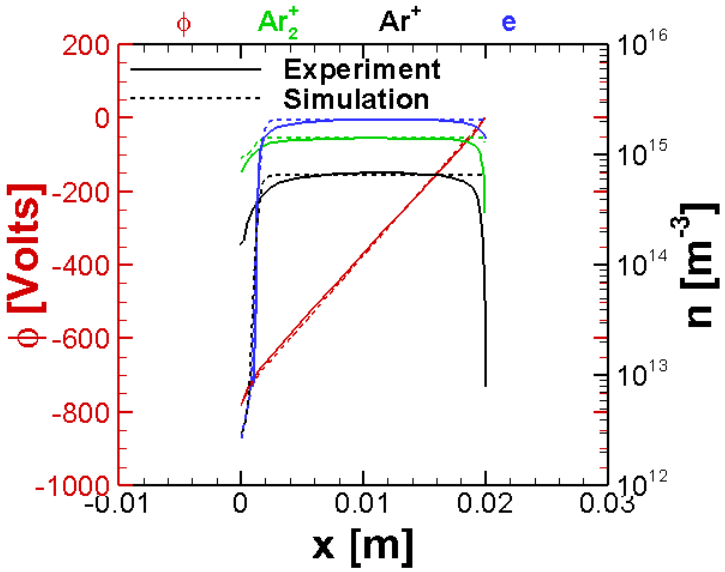

Figure 3.5 Simulation data taken at the peak of the pulse (78.5 ns) and matched to previous experimental data

We examined PGRS generation in argon and air as a function of V_p and σ for an applied electric pulse with time dependence given by Equation (2.1). Figures 3.4 and 3.5 show species formation and electric potential across the gap with increasing V_p by fixing $\sigma = 3$ ns and $p = 3$ Torr, and considering $V_p = 450$ V, 850 V and 1250 V. Figures 3.6 and 3.7 shows that increasing V_p increases n_e and n_i for argon and air. Figures 3.6(a) and 3.7(b) show n_e and n_i at peak V_p ($t = 78.5$ ns) and after voltage decay ($t = 150$ ns), respectively. Figures 3.7, 3.8, and 3.9 similarly assess the spatial profies of potential ϕ, n_e, and n_i under various conditions. Figures 3.6(a), 3.7(a), 3.8(a), and 3.9(a) demonstrate the sheath formation and separation of the ions and electrons at the EP peak because the electrons move faster than the ions, causing n_e (solid) and n_i (dashed) to diverge before returning to quasineutrality ($n_e \approx n_i$) in the bulk. After the EP, Figures 3.6(b), 3.7(b), 3.8(b), and 3.9(b) show $n_e \approx n_i$ across the gap.

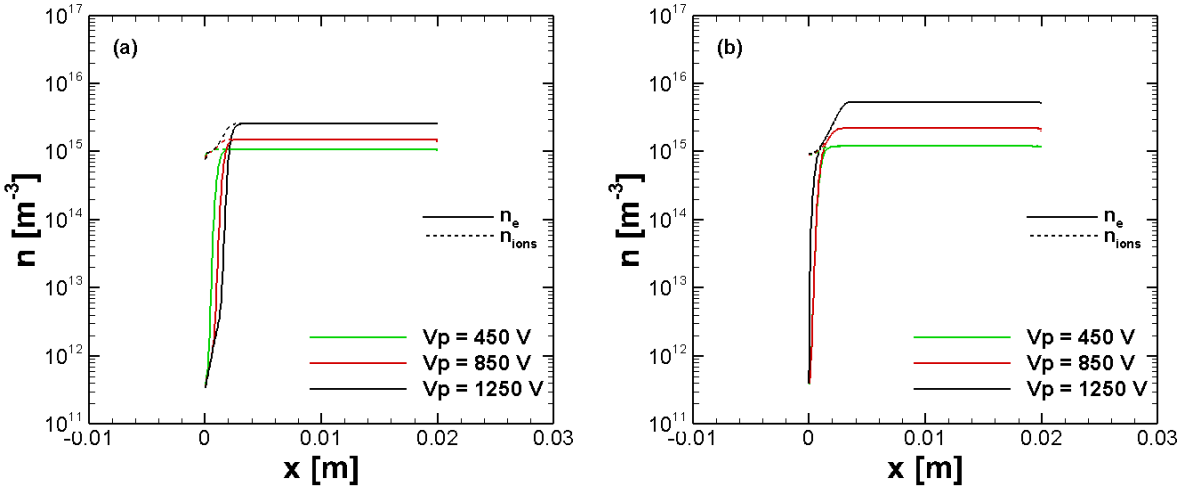

Figure 3.6 Argon model: (a) Spatial profile of electron (n_e) and ion (n_i) density showing that each increases with increasing applied voltage at the peak voltage (78.5 ns); (b) Spatial profile of n_e and n_i after the electric pulse (150 ns) showing that $n_e = n_i$ and each density is higher than at the peak.

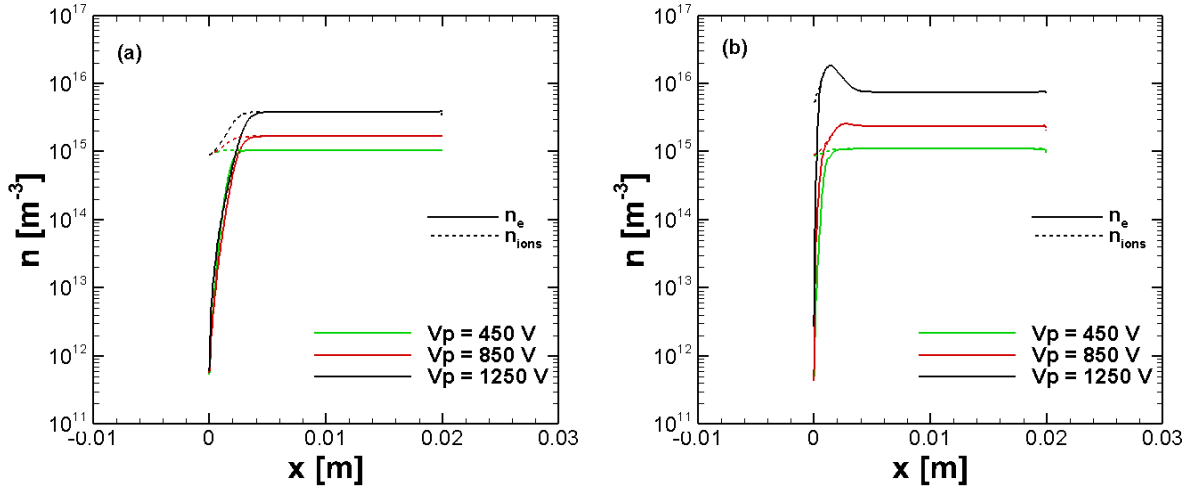

Figure 3.7 Air model: (a) Spatial profile of electron (n_e) and ion (n_i) density showing that each increases with increasing applied voltage at the peak voltage (78.5 ns); (b) Spatial profile of n_e and n_i after the electric pulse (150 ns) showing that the magnitude increases with peak voltage, $n_e = n_i$, and each density is higher than at the peak.

Figures 3.8 and 3.9 assess the impact of varying σ for $V_p = 850$ V, $p = 3$ Torr, and $\sigma = 1$, 3, and 6 ns for argon and air. For both gases, increasing σ for a fixed V_p increased ionization. At low levels of ionization and voltage, we predict that this trend remains until pulses become repeated. Argon

was more sensitive to voltage with a higher concentration of species compared to varying pulse width. Air exhibited more sensitivity to pulse width after the EP and showed more ionization than argon.

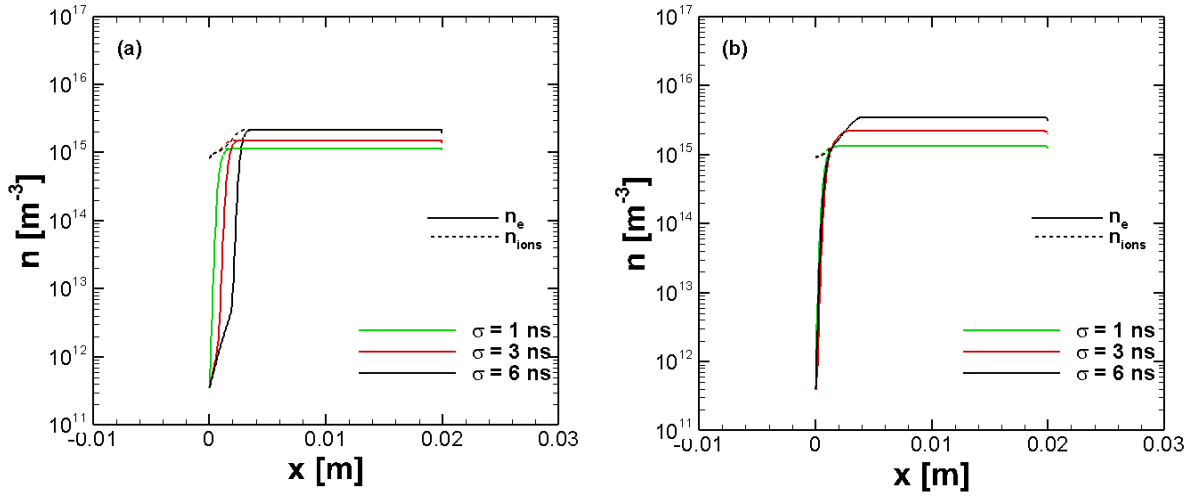

Figure 3.8 Argon model: (a) Spatial profile of electron (n_e) and ion (n_i) density showing that each increases with increasing pulse width σ at the peak voltage (78.5 ns); (b) Spatial profile of n_e and n_i after the electric pulse (150 ns) showing that $n_e = n_i$ and each density is higher than at the peak.

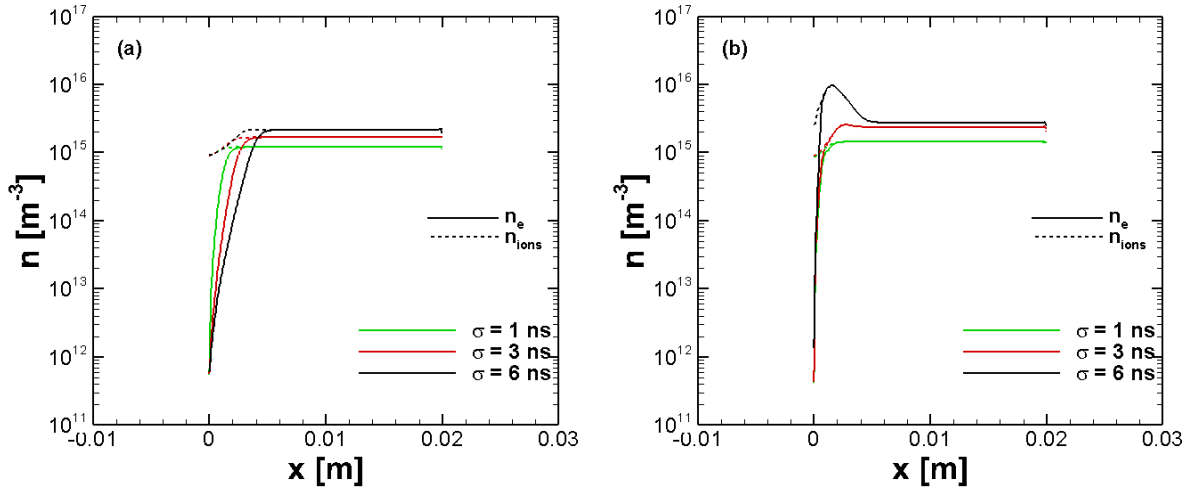

Figure 3.9 Air model: (a) Spatial profile of electron (n_e) and ion (n_i) density showing that each increases with increasing pulse width σ at the peak voltage (78.5 ns); (b) Spatial profile of n_e and n_i after the electric pulse (150 ns) showing that $n_e = n_i$ and each density is higher than at the peak.

3.1.3 Effect of Pressure

Device and experiment scalability are critical for parameter selection. For instance, Paschen derived the condition for avalanche formation as a function *pd* for DC discharges and most conditions.[18,81]; for microscale gaps at atmospheric pressure, field emission drives breakdown and the voltage scales with *d* at a fixed pressure [18,21]. To assesses the relevance of *pd* scaling with our simulation, we fixed *pd* = 12 Torr·cm and determined the potential ϕ across the gap as a function of normalized position *x*/*d* for various *p* and *d*. Figure 3.10 shows that the sheath edge occurs at d_s ≈ 3mm for both argon and air. The potential in the cathode remains the same and we observe a similar voltage fall for fixed *pd* at different values of *p* and *d*. For argon, the peak ϕ increases with decreasing *d* until *d* ~ 3 cm, at which point changing *d* induces negligible change in ϕ. The normalized location (*x*/*d*) of the peak ϕ also increases with decreasing *d* until *d* ~ 3 cm. Unlike argon, decreasing *d* reduces the peak ϕ for air.

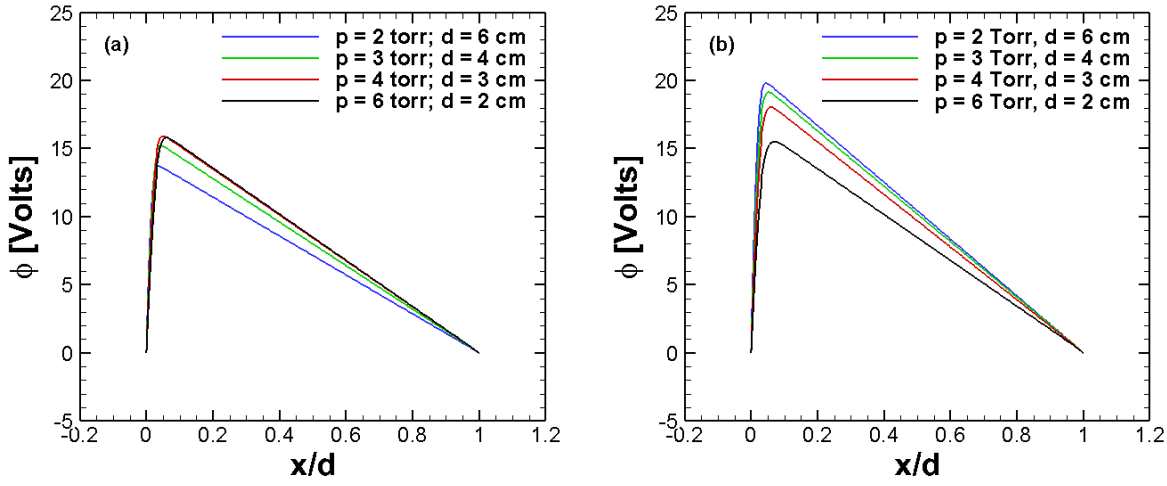

Figure 3.10 Potential profile (φ) after voltage decay (150 ns) for fixed *pd* = 12 Torr·cm for (a) argon and (b) air.

To directly examine the effect of pressure, we next considered ϕ as a function of *d* for fixed *d* = 2 cm and *p* = 2 Torr, 3 Torr, and 6 Torr. Figure 3.11 shows that that voltage fall occurs at higher pressures and the number densities see small increases from a higher increased potential. This methodology of scaling *p* and *d* is how we formulate the next set of simulations in this thesis.

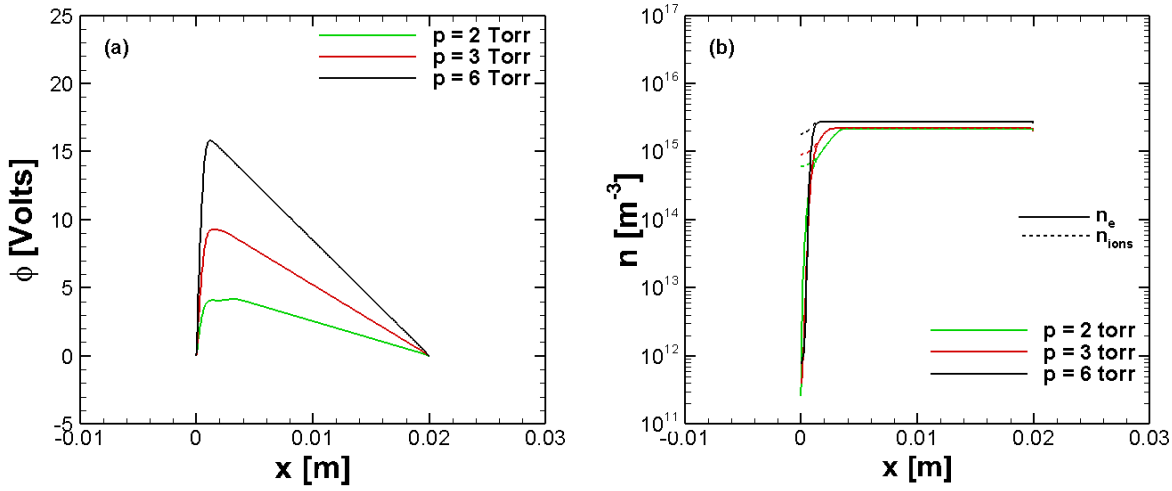

Figure 3.11 (a) Spatial profile of (a) potential ϕ and (b) electron number density n_e for argon. Both ϕ and n_e increase with increasing pressure.

We note that the current results did not exhibit *pd* scaling for a NPP discharge, indicating that they require different scaling and assessment than Paschen's classical experiment. Although, the methodology of scaling and testing scaling laws is important for the next part of this thesis we leave this section for investigation at a later time.

3.1.4 Scaling Pulse Parameters for a Single Pulse

A common consideration when designing pulse generators concerns selection of pulse width and voltage. In many applications, engineers strive to understand the scalability of pulsed power system parameters, often power or energy delivered to the load, to induce a desired phenomenon. Such understanding helps guide experimentalists in selecting appropriate pulsed power architectures to balance expense and desired outcome. Although the results above show that the conductivity of the generated plasma will most likely change ϕ, n_e and n_i across the gap compared to a simple scaling parameter, the tool presented here can provide a screening tool to characterize the limitations of these simple estimates to provide insight into parameter selection. For instance, this simulation may provide guidance into the values of V_p and σ needed to achieve a given n_i or n_e and whether similar behavior may be achieved with a lower V_p and higher σ, which may yield a less expensive and more compact pulsed power architecture.

To assess the scaling of the energy of the applied pulse, we start by defining the instantaneous power delivered by the pulse as $P_d = V_{applied}^2/R_p$, where R_p is the initial resistance of the gap containing either argon or air. Assuming that R_p is fixed for a given condition (it will naturally change upon applying the pulse, but parameter selection is usually based on this simple initial assumption), the energy delivered to gap is given by

$$Q = \int_{-\infty}^{\infty} \frac{V_p^2}{R} \exp\left\{-\frac{2(t-t_0)^2}{\sigma^2}\right\} dt = \frac{V_p^2 \sigma}{R}\sqrt{\frac{\pi}{2}}, \tag{3.5}$$

which shows that the energy is directly proportional to V_p^2 and σ. Figure 3.12(a) shows that doubling V_p doubles the area under the curve; Figure 3.12(b) shows that doubling σ doubles the area under the curve.

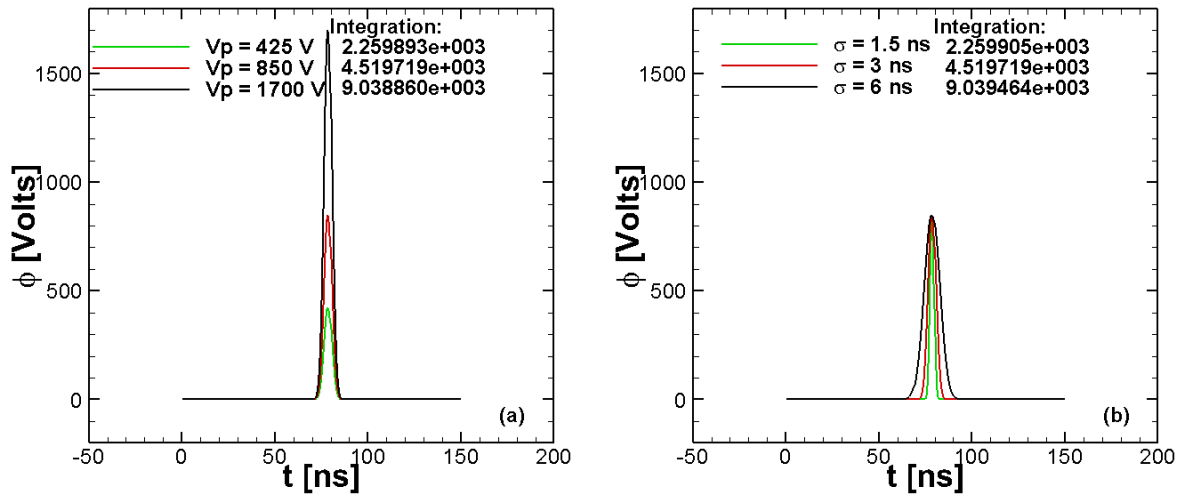

Figure 3.12 Impact of changing pulse parameters on potential ϕ. (a) Fixing pulse width σ and changing peak voltage V_p shows that increasing V_p increases peak ϕ. (b) Fixing V_p and increasing σ induces a concomitant increase in the width of ϕ.

Since R_p is assumed constant at the start of the EP, setting $V_p^2\sigma$ to a constant will demonstrate the behavior with regards to variation in V_p and σ for a fixed energy delivered to the system. This will allow the ability to distinguish the impact of σ on n_e and n_i since it defines a standard invariant quantity of total delivery to the gas. Figure 3.13 shows the instantaneous power delivered to the

gap for a constant energy input ($Q_{green} = Q_{red} = Q_{black}$) based on our variation of V_p and σ. Figures 3.14 and 3.15 show for fixed $V_p^2\sigma$, shorter duration EPs with higher voltage induced higher n_e and n_i. Interestingly, reducing σ below ~3 ns reduced the increase in n_e and n_i with further decrease in σ. Although continuing to reduce σ will most likely continue to increase n_e and n_i, the practical improvement with increased device cost and complexity would likely make it impractical. Thus, this simulation provides guidance on the practical limitations of pulse generator design for optimizing EP parameters to maximize PGRS.

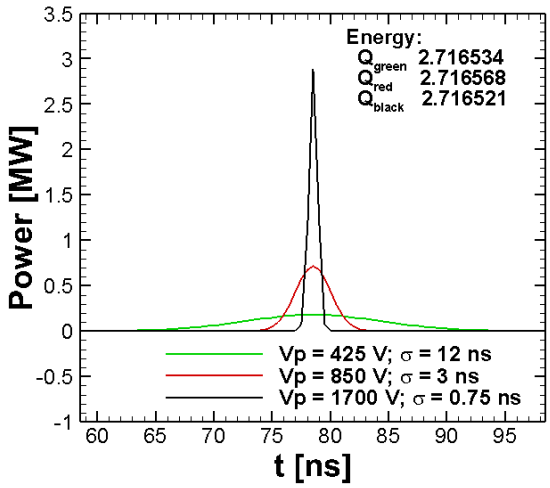

Figure 3.13 Instantaneous power applied across the gap as a function of time with the total energy across the gap fixed at 2.72 MW. The peak power across the gap increases with decreasing σ.

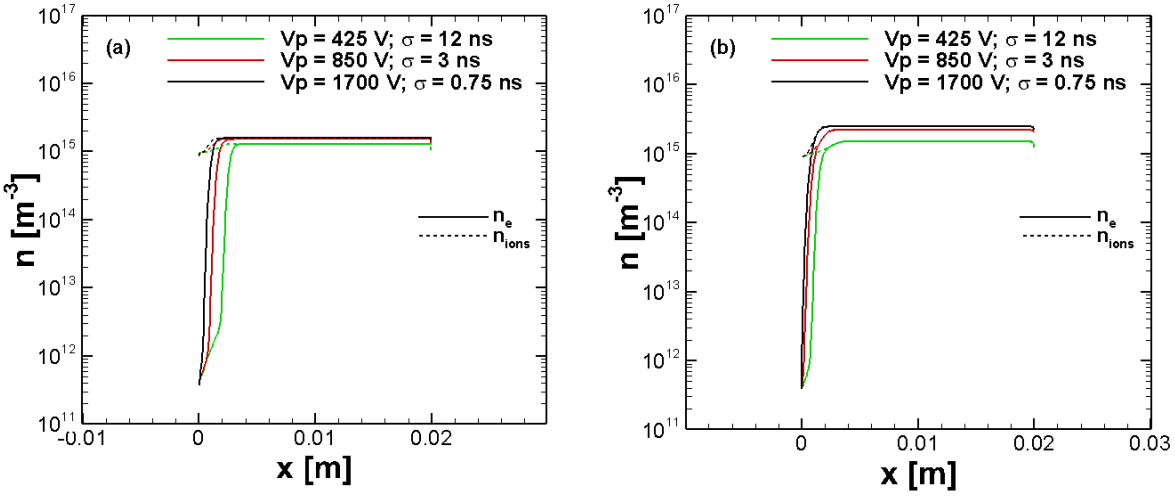

Figure 3.14 Spatial profile of electron (n_e) and ion (n_i) density for argon for electric pulses with fixed energy (constant $V_p^2\sigma$) (a) at the peak voltage (t = 78.5 ns) and (b) after the electric pulse (150 ns). Reducing σ increases n_e and n_i, although the increase becomes less significant with further reductions in σ. This suggests a practical limit to reducing σ for increasing n_e and n_i.

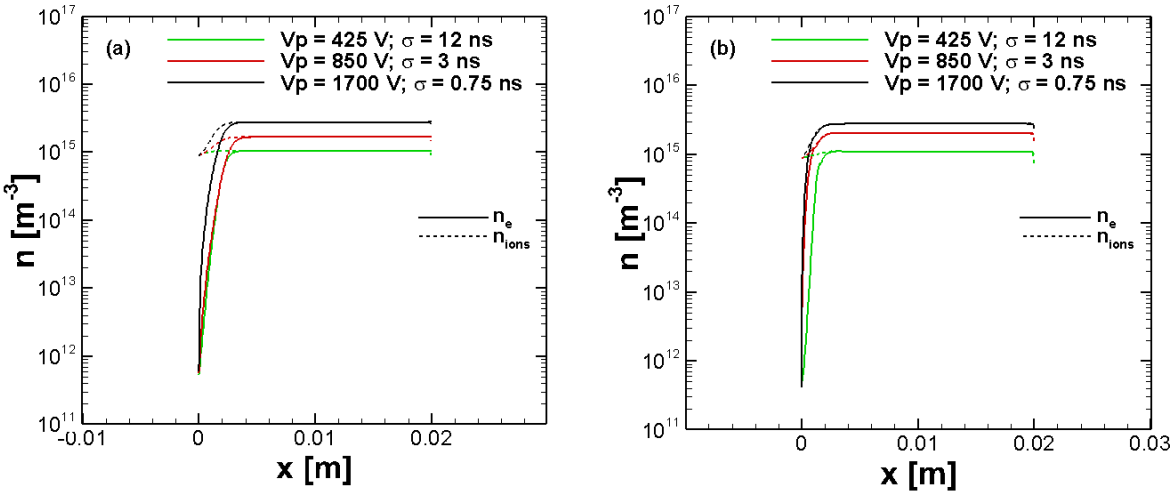

Figure 3.15 Spatial profile of electron (n_e) and ion (n_i) density for air for electric pulses with fixed energy (constant $V_p^2\sigma$) (a) at the peak voltage (t = 78.5 ns) and (b) after the electric pulse (150 ns). Reducing σ increases n_e and n_i, although the increase becomes less significant with further reductions in σ. This suggests a practical limit to reducing σ for increasing n_e and n_i.

3.2 Multiple Pulse Simulations

This section extends the application of this model to repetitive pulses. Repetitive pulses are highly appealing for plasma devices since they can reduce the cost expense for generating more ionized

and excited species. We extend the EP parameters study for repetitive NPP and compare repetitive pulsing to a single NPP. For the current model and its capabilities, this section remains difficult numerically because of the time scales of the discharge and the effect of electron temperature; however, it provides insight into the implications of multiple pulses on parameter that determine the energy delivered. The time between EPs (or the repetition rate) is a particularly critical parameter for pulse generator design since increasing repetition rate increases the power requirements of the pulse generator and the resulting expense. We also examine the electron temperature at different pulse repetition rates. We did not report this for a single EP and how this effects the numerical solution.

3.2.1 Scaling Pulse Parameters for Multiple Pulses

This section examines the PGRS generation in argon and air as a function of V_p and σ for two and five applied EPs given by Equation (2.1) with nominal parameters of V_p = 850 V, p = 3 Torr, and σ = 3 ns.

Figures 3.16 and 3.17 look at fixing σ = 3 ns and considering V_p = 450 V, 850 V and 1250 V which shows that increasing V_p causes n_e and n_i to increase for argon and air. Figures 3.16(a) and 3.17(b) show n_e and n_i after voltage decay (t = 150 ns times number of EPs) after either two or five EPs, respectively. Figures 3.16 - 3.19 show the spatial profies of potential ϕ, n_e, and n_i under various conditions.

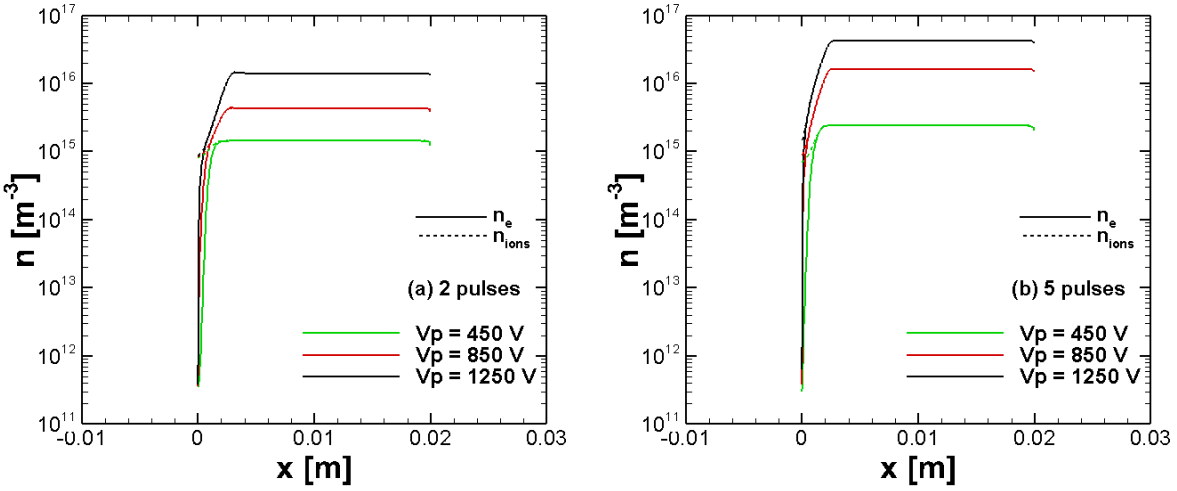

Figure 3.16 Spatial profile of electron (n_e) and ion (n_i) density for argon with fixed σ = 3 ns, p = 3 Torr and ν = 6.7 MHz. Shows that density increases with more pulsing and increased applied voltage V_p after the voltage decay for (a) two pulses and (b) five pulses.

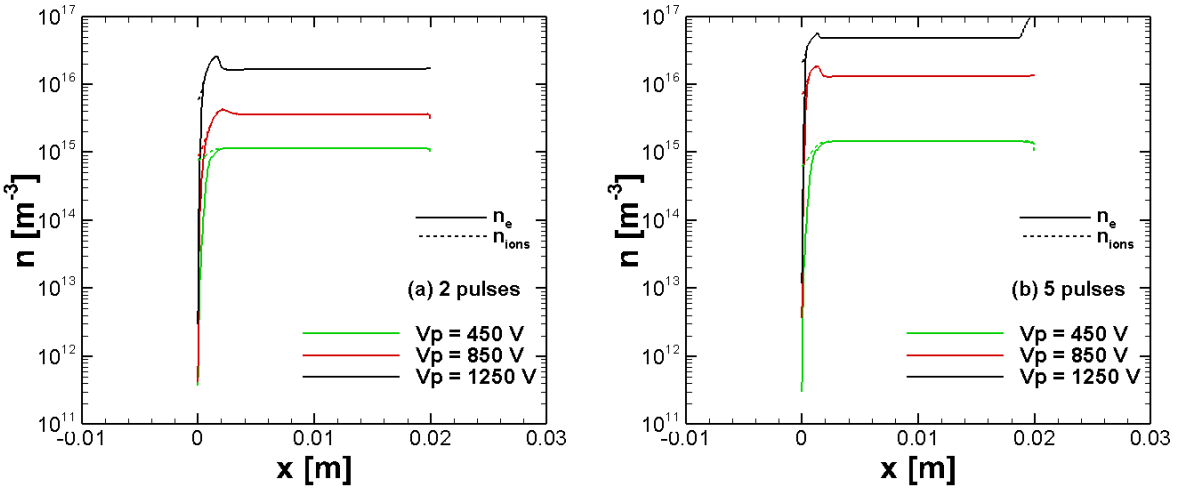

Figure 3.17 Spatial profile of electron (n_e) and ion (n_i) density for air with fixed σ = 3 ns, p = 3 Torr and ν = 6.7 MHz following (a) two and (b) five pulses. Both n_e and n_i increase with more pulsing and increased applied voltage V_p after voltage decay.

Figures 3.17 and 3.18 assess the impact of varying σ for V_p = 850 V, p = 3 Torr, and σ = 1, 3, and 6 ns for argon and air, respectively. For both gases, increasing σ for a fixed V_p increased ionization. However, applying five EPs with σ = 3 ns induced as much ionization as setting σ = 6 ns,

suggesting a saturation in species generation for sufficiently long duration EPs. Further simulations may determine the potential for this saturation to occur for shorter σ with more EPs.

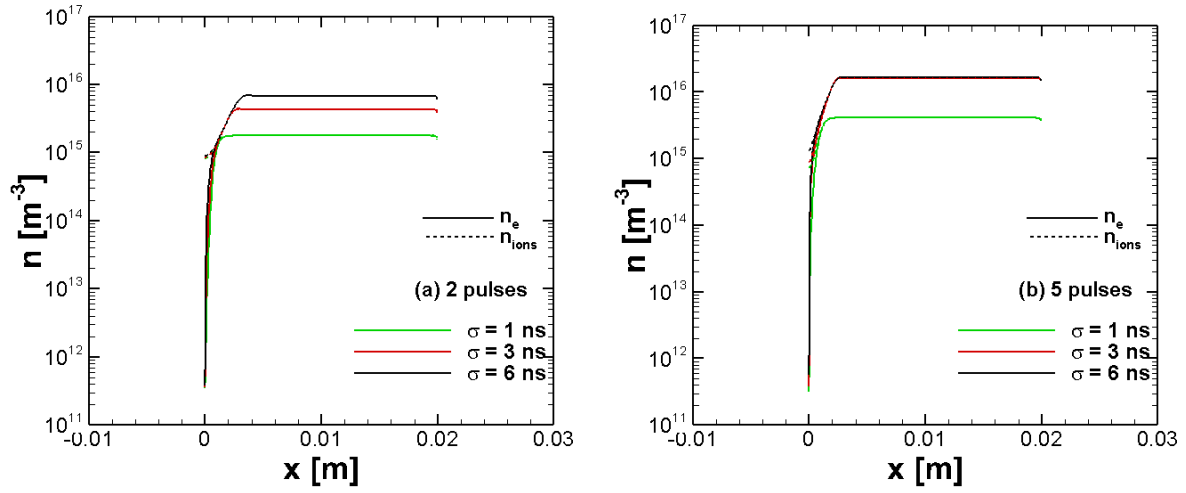

Figure 3.18 Spatial profile of electron (n_e) and ion (n_i) density for argon with fixed V_p = 850 V, p = 3 Torr and ν = 6.7 MHz after (a) two and (b) five pulses. Electron (n_e) and ion (n_i) density increases with more pulsing and increased σ after the voltage decay. After five pulses, there is no visible difference between σ = 3 ns and σ = 6 ns.

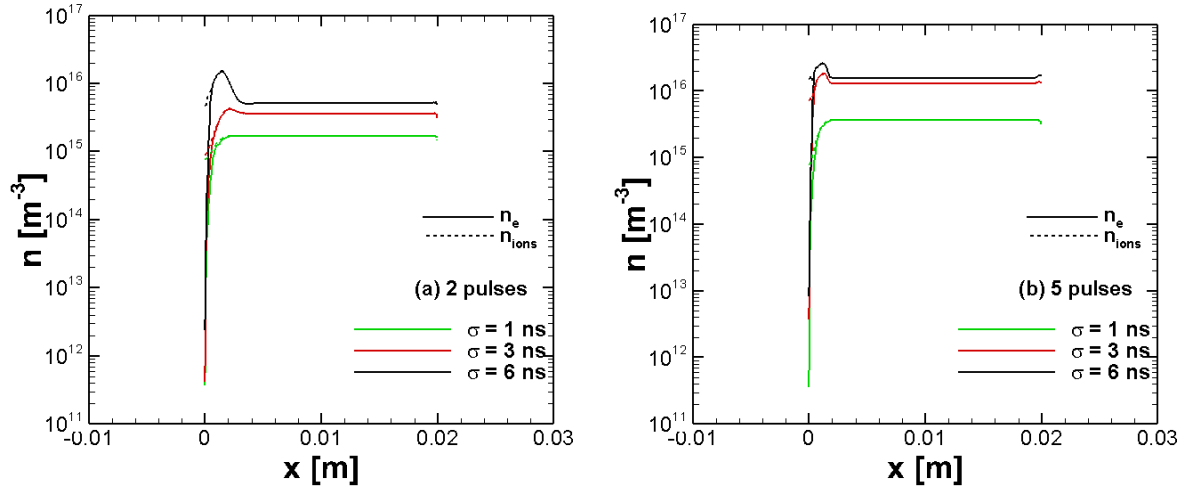

Figure 3.19 Spatial profile of electron (n_e) and ion (n_i) density for air with fixed V_p = 850 V, p = 3 Torr and ν = 6.7 MHz after (a) two and (b) five pulses. Electron (n_e) and ion (n_i) density increases with more pulsing and increased σ after the voltage decay. After five pulses, there is no visible difference between σ = 3 ns and σ = 6 ns.

3.2.2 Energy Scaling for Multiple Pulses

Section 3.1.4 examined the implications of changing σ for a fixed applied EP energy (fixed $V_p^2\sigma$) to determine a set of scaling laws for a single EP. This section applied the same methodology to examine the results as a function of the repetition rate. For the single EP, applying an EP with the same energy at lower σ resulted in greater peak instantaneous power delivered and a greater n_e and n_i until $\sigma \lesssim 3$ ns. For lower σ, further reductions induce no significant increase in PGRS. The question becomes whether we can induce similar behavior for repetitive EPs and, if so, how does changing the pulse repetition rate influence this behavior.

Analogous to our single EP study, we test argon and air for a constant $V_p^2\sigma$ for two and five EPs. Figure 3.20(a) and 3.20(b) show n_e and n_i for argon with for two and five EPs, respectively. Overall, the n_e and n_i are higher after five EPs and two EPs, indicating a cumulative effect with applying more EPs of the same energy. As for a single EP at a constant $V_p^2\sigma$, reducing σ results in higher n_e and n_i. For two EPs, the increase in n_e and n_i slows down from $\sigma = 3$ ns to 0.75 ns, but there is a much more noticeable increase than for a single EP. Applying five EPs causes a more substantial increase going from $\sigma = 3$ ns to 0.75 ns. Clearly, the increase in n_e and n_i for decreasing σ increases as more EPs are applied; however, this rate of this increase with decreasing σ still decreases. Thus, at some point, we speculate that applying more EPs will eventually result in a plateau where reducing σ no longer increases n_e and n_i. The question becomes the pulse repetition rate (time between EPs) and number of EPs at which this occurs.

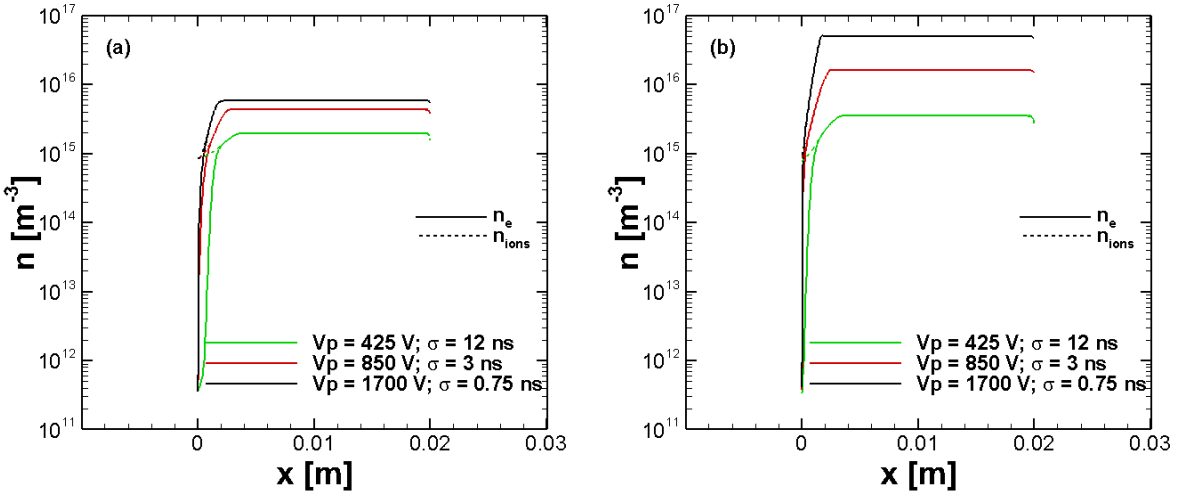

Figure 3.20 Argon model: Spatial profile of electron (n_e) and ion (n_i) density showing the increased amount of species occurs with a higher voltage and a shorter pulse width at the peak following (a) two and (b) five electric pulses.

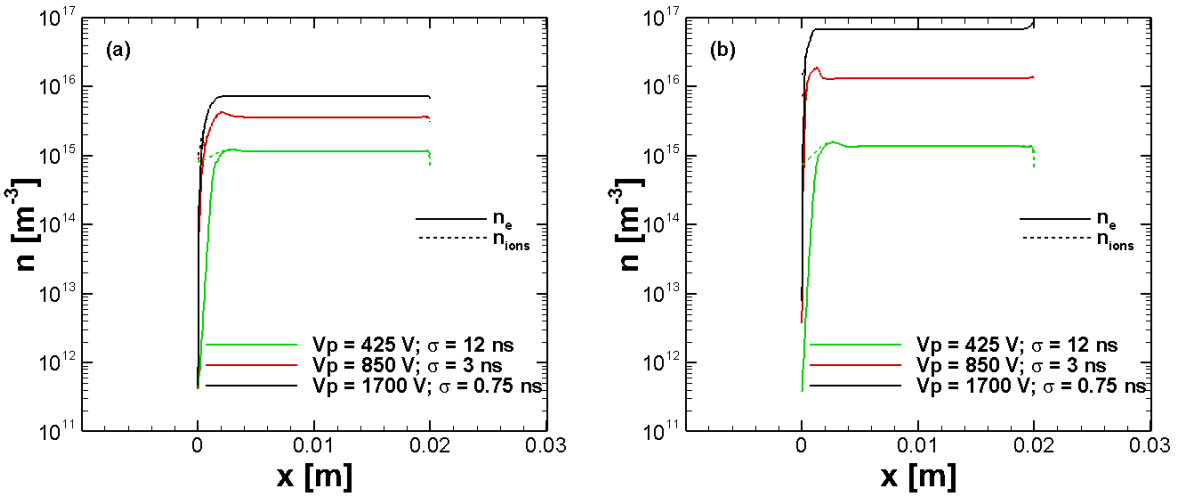

Figure 3.21 Air model: Spatial profile of electron (n_e) and ion (n_i) density showing the increased amount of species occurs with a higher voltage and a shorter pulse width at the peak following (a) two and (b) five electric pulses.

3.2.3 Effect of Electron Temperature

The electron temperature T_e, which describes the amount of energy and electron has, is a critical parameter for characterizing ionization of particles. In DC discharges, T_e ~1eV. Ionization becomes more efficient with increasing mean electron energy. This can occur in the range of 100

< T_e < 1000 eV. This amount of energy can be achieved by injecting an electron beam or by applying a highly repetitive NPP. In NPPs, the potential fluctuates due to the fluctuating production of more ions and electrons, and the increased volume of the electrons can act similarly to an electron beam. The potential for T_e to reach such high values for the NPP makes obtaining the numerical solution for repetitive pulsing difficult. Many simulations begin by benchmarking to a constant T_e. For nonequilibrium discharges, T_e > 1eV and the ion temperature T_i should remain around room temperature. The electron temperature is linked to the energy equation and the next step up from the one moment model is to solve the energy equation. Coupling the energy equation to the continuity equation and Poisson's equation is not always apparent and can increase the difficulty of the simulation.

One common simplification involves approximating T_e through experimental data, although this can yield poor results. Instead of using the full energy equation, T_e is based on the local electric fields. As shown in Table 2.4 and 2.5 the electron temperature appears in the calculation of the reaction rates. Because BOSLIG+[71] is already established as a two-term approximation to the Boltzmann equation, it is easily integrated with other techniques to find the EEDF and various swarm parameters, which are calculated by inputting the cross-sectional data from different databases that have been contributed by different groups. The databases can be difficult to navigate and difficult to ensure the use of good data depending on a specific experiment. Although BOLSIG+ has some drawbacks, it is currently the best tool and sufficient for our purpose. To incorporate these results into the simulation, we curve-fit the BOLSIG+ data at the appropriate electron temperature, as done by Piskin [14] for similar simulations.

Crashes of the code occurred after many successive pulses due to high electron densities and the rapidly varying electric field. This section attempts to understand the electron temperature by varying pulse frequency. Figure 3.22 shows the electron temperature over time. The electron temperature continues to rise after each successive pulse. Three pulse periods were tested to see if the electron temperature would decay. Figure 3.22 shows pulse periods of T = 150 ns, 675 ns, and 1500 ns, and the electron temperature after five pulses. The pulse frequencies tested showed no immediate decay of the electron temperature and require and increased amount of time between successive pulses. Future studies will consider repletion rates on the order of kHz.

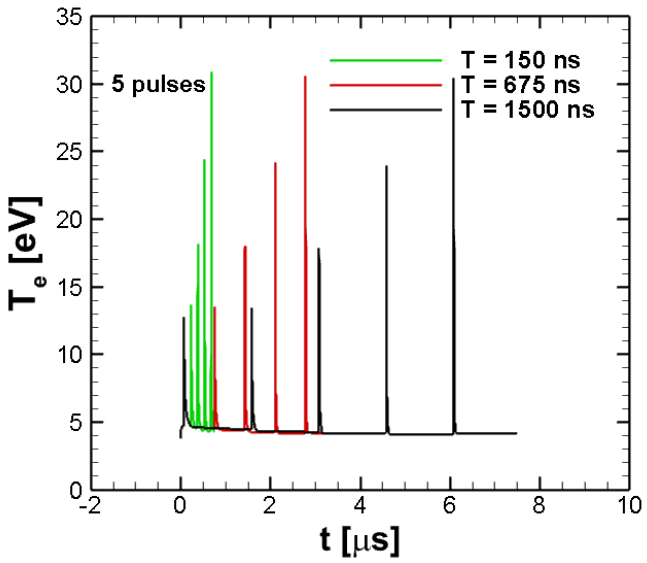

Figure 3.22 Electron temperature as a function of time with varying pulse frequencies for 5 pulses

3.3 Summary

This chapter presents a simulation of a nanosecond pulse discharge to calculate the concentrations of excited and ionized species and the induced electric field in a gas discharge. The model implemented the DD approximation and solved a single moment of the Boltzmann equation for simplicity and computational efficiency. We applied this model to examine the effect of single and multiple pulses and the EP parameters on argon and air chemistry. Ionization continued to increase after applying a Gaussian electric pulse. Calculations at the peak of the pulse and after completing the pulse period showed the separation of ions and electrons early in the pulse near the cathode, confirming sheath formation, and the subsequent return to quasi-neutrality after the voltage decay. For a fixed pressure and duration, electron and ion densities increased with increasing voltage. For a fixed applied voltage and pressure, increasing the pulse width increased electron and ion densities.

The effects of fixing the product of pressure and gap distance were studied for the two models. The potential in the region of the cathode stayed the same for constant *pd*. For a fixed *d*, the voltage fall increased with increasing *p*. For a fixed pulse energy delivered to the gap, given by fixed $V_p^2\sigma$, electron and ion number densities both increased with decreasing σ; however, the rate of this

increase of number density decreased for $\sigma \lesssim 3$ ns, suggesting a practical limit. Applying multiple EPs yielded similar results to a single EP. Applying either two or five EPs with various σ and the same total energy, we observed that the rate of increase of n_e and n_i decreased with decreasing σ as in the single EP case; however, the difference from $\sigma = 3$ ns to $\sigma = 0.75$ ns increased as we applied more EPs. This suggests that we can enhance n_e and n_i with lower σ for multiple EPs; however, this behavior requires a sufficiently high repetition rate, which can be expensive to achieve. Nevertheless, more detailed studies with longer EP trains may provide insight into practical limitations for enhancing n_e and n_i with repetitive pulsing that guide EP parameters.

4. CONCLUSION

This section summarizes the work completed and conclusions drawn in this thesis for a 1D simulation of gas discharge physics following nanosecond EPs. This section recommends future work and discusses techniques that could be developed for computational efficiency and improvements of the physical model.

4.1 Summary

The first chapter begins as a review of plasmas: what constitutes a plasma, how plasmas are formed, and the different types of plasmas that can form. Plasmas form when the Debye length is smaller than the dimensions of the plasma, the number of electrons in the Debye sphere is very high and when the electron-neutral collision frequency is smaller than the plasma frequency. Different types of plasmas can be produced with either thermal or electrical input. This sets up the analysis for nanosecond low temperature gas discharge, in which the mechanisms behind electrical gas discharges are discussed, the applications that go along with them, and how to achieve a good numerical solution with the given challenges.

The strong nonlinearity of the problem makes the PS stiff, which necessitates high temporal and spatial resolutions to capture the limiting processes. Ionization in the cathode sheath limited the time step for the physical processes. Numerical time scales that limited this problem were also the CFL timescale and the dielectric relaxation time scale. Additionally, PSs were compared to a CFD solver and a discussion of how the two solvers could be coupled was presented. While a fully coupled solution with CFD would require large computational demands, a loosely coupled model is possible.

A review of numerical models such as kinetic and fluid models was presented to justify the selection of a fluid model, which provided a simpler description of the Boltzmann's equation and explained the utilization of the one moment model. Combining the explicit discretization of the governing equation with Scharfetter-Gummel's approach for treating the flux provided a satisfactory solution with relatively low computational expense. Additionally, the Scharfetter-

Gummel approach specifically captured regions that were either highly drift dominated or highly diffusion dominated. Model development began at lower pressures because it was easier to obtain a diffuse homogenous plasma. Validation of this model was compared to another model that has been developed for an NPP in argon.

A model for a nanosecond pulse discharge was developed to test various EP parameters. The goal was to analyze ionized species and the induced electric field in a gas discharge as a function of EP parameters for argon and air chemistry. Single pulse analysis was representative of an experiment and the model was fit to the experimental data. Data were analyzed at two instances of the pulse: at the peak of the pulse, and after the period. Continued ionization and an increase in density were seen after the EP decayed away.

The initial pulse parameter study showed increasing the peak voltage for a fixed pulse duration, increased the amount of species. Similarly, increasing the pulse width for a fixed peak voltage, increased the amount of species. When studying the product of pressure and gap distance the potential in the region of the cathode stayed the same when *pd* was constant. When pressure increased and distance was kept constant the we saw the voltage fall increase and the amount of species increase.

Single and multiple pulses showed n_e and n_i formation for reduced σ for fixed applied energy. The densities n_e and n_i for multiple pulses continued to increase for lower σ as compared to a single EP. This suggests another benefit of repetitive EPs and the need for a more detailed analysis of more EPs and lower σ to optimize EP parameters, including σ, V_p, and time between EPs. Since designing pulse generators with low σ and high V_p is more complicated and expensive, these results provide a general parameter space for the lowest σ most likely to lead to the most useful results for practical applications.

For a 1D NPP discharge, we can see general discharge behavior such as sheath formation, the sharp gradients in the region of the cathode and a region of quasi-neutrality in the positive column. This model agrees well with other simplified models that have been developed.

4.2 Future Work

Plans for future work are discussed in this section. One can understand the complex nature of this evolving problem when discussing the potential paths forward. This 1D model provided many challenges but gives a first order understanding of the implications of EP parameters on species formations; however, these simplifications are inadequate for many experimental setups. Specifically, the 1D planar model is accurate for a uniform electric field and discharge; however, actual experiments often use a pin-to-plate or pin-to-pin geometry, which makes the electric field and subsequent species formation non-uniform. Large amounts of non-uniformity are also evident in fluid dynamics and must also be considered when coupling to a flow solver.

Because of these common geometries, modeling for specific applications, such as combustion or flow control, necessitates extending the model to 2D. Although specific 1D problems often already have large computational requirements, the 2D representation is more accurate for the given applications, particularly those at atmospheric pressure, which will add to the computational expense. Specifically, atmospheric pressure requires refined spatial scales to capture the discharge profile because the sheath thickness decreases with increasing pressure. The simulations reported in this thesis were conducted at low pressure (2-6 Torr) as a proof of principle for easier computation and should be extended to test higher pressure cases. More experimental data is also available at atmospheric pressure.

Thus, the specific goal for subsequent work is to extend the dimensions to 2-D for a pin-to-pin geometry. Although this geometry necessitates 2-D simulations, assuming an axisymmetric geometry can facilitate the calculation. By using sharp tip electrodes (e.g. corona discharges) one can achieve high electric fields and consequently produce high concentrations of species, which makes them appealing for applications such as combustion enhancement. Developing an axisymmetric model for a sharp tip geometry will permit the elucidation of EP parameters for species generation and the ultimate examination of other discharge geometries. This will also enable the loose coupling of the modeling to the CFD model.

Finally, more analysis should be done on the plasma chemistry. The highest fidelity model would include a complete set of species and reactions but is almost computationally impossible. It is

understood that some species and reactions are not as effective as others and numerous reactions should be examined at different discharge conditions. Developing a collection of the most effective reactions to include or exclude at different discharge conditions would be extremely helpful to the community.

REFERENCES

[1] M. Friedman, V. Serlin, A. Drobot, and A. Mondelli, IEEE Trans. Plasma Sci. **14**, 201 (1986).

[2] E. Moreau, J. Phys. D. Appl. Phys. **40**, 605 (2007).

[3] M.G. Kong, G. Kroesen, G. Morfill, T. Nosenko, T. Shimizu, J. Van Dijk, and J.L. Zimmermann, New J. Phys. **11**, 115012 (2009).

[4] Y. Ju and W. Sun, Combust. Flame **162**, 529 (2015).

[5] F. Chen, *Plasma Physics and Controlled Fusion*, 2nd ed. (Springer Science+Buisness Media, New York, 2010).

[6] J.A. Bittencourt, *Fundamentals of Plasma Physics*, 3rd ed. (Springer Science+Buisness Media, New York, 2004).

[7] I. Adamovich, S.D. Baalrud, A. Bogaerts, P.J. Bruggeman, M. Cappelli, V. Colombo, U. Czarnetzki, U. Ebert, J.G. Eden, P. Favia, D.B. Graves, S. Hamaguchi, G. Hieftje, M. Hori, I.D. Kaganovich, U. Kortshagen, M.J. Kushner, N.J. Mason, S. Mazouffre, S. Mededovic Thagard, H.-R. Metelmann, A. Mizuno, E. Moreau, A.B. Murphy, B.A. Niemira, G.S. Oehrlein, Z.L. Petrovic, L.C. Pitchford, Y.-K. Pu, S. Rauf, O. Sakai, S. Samukawa, S. Starikovskaia, J. Tennyson, K. Terashima, M.M. Turner, M.C.M. van de Sanden, and A. Vardelle, J. Phys. D. Appl. Phys. **50**, 323001 (2017).

[8] J.J. Wang, K.S. Choi, L.H. Feng, T.N. Jukes, and R.D. Whalley, Prog. Aerosp. Sci. **62**, 52 (2013).

[9] M. Laroussi, IEEE Trans. Plasma Sci. **43**, 703 (2015).

[10] A.M. Howatson, in *An Introd. to Gas Discharges*, 2nd ed. (Pergamon Press Inc., New York, 1965), pp. 1–5.

[11] G. Salet, London, Edinburgh, Dublin Philos. Mag. J. Sci. **1**, 331 (1876).

[12] G.F. Knoll and H.W. Kraner, *Radiation Detection and Measurement*, 4th ed. (John Wiley & Sons, Inc., 1981).

[13] A. Von Keudell and V. Schulz-Von Der Gathen, Plasma Sources Sci. Technol. **26**, 11301 (2017).

[14] T. Piskin, Numerical Simulations of Gas Discharges for Flow Control Applications, Purdue University, West Lafayette, IN, 2019.

[15] A.M. Loveless and A.L. Garner, Appl. Phys. Lett. **108**, 234103 (2016).

[16] A.M. Loveless and A.L. Garner, Phys. Plasmas **24**, 113522 (2017).

[17] Y.P. Raizer, *Gas Discharge Physics* (Springer-Verlag, New York, 1987).

[18] A.L. Garner, A.M. Loveless, J.N. Dahal, and A. Venkattraman, IEEE Trans. Plasma Sci. **48**, 808 (2020).

[19] D.B. Go and A. Venkattraman, J. Phys. D. Appl. Phys. **47**, 503001 (2014).

[20] Y. Fu, P. Zhang, J.P. Verboncoeur, and X. Wang, Plasma Res. Express **2**, 013001 (2020).

[21] A.M. Loveless, G. Meng, Q. Ying, F. Wu, K. Wang, Y. Cheng, and A.L. Garner, Sci. Rep. **9**, 5669 (2019).

[22] A. Starikovskiy and N. Aleksandrov, Prog. Energy Combust. Sci. **39**, 61 (2013).

[23] L. Bromberg, D.R. Cohn, A. Rabinovich, N. Alexeev, A. Samokhin, R. Ramprasad, and S. Tamhankar, Int. J. Hydrogen Energy **25**, 1157 (2000).

[24] Y. Ju and W. Sun, Prog. Energy Combust. Sci. **48**, 21 (2015).

[25] I. V. Adamovich and W.R. Lempert, Plasma Phys. Control. Fusion **57**, (2015).

[26] A.A. Konnov, Combust. Flame **152**, 507 (2008).

[27] Z. Yin, A. Montello, C.D. Carter, W.R. Lempert, and I. V. Adamovich, Combust. Flame **160**, 1594 (2013).

[28] R.B. Bird, W.E. Stewart, and E.N. Lightfoot, *Transport Phenomena* (John Wiley & Sons Inc., 2002).

[29] C.L. Fefferman, *Existence and Smoothness of the Navier–Stokes Equation* (Clay Mathmatical Institute, American Mathematical Society, Cambridge MA, Providence RI, 2006).

[30] M. Kerho and B. Kramer, in *41st AIAA Aerosp. Sci. Meet. Exhib.* (Reno, Nevada, 2003), pp. 1–18.

[31] J. Poggie, Int. J. Comut. Fluid Dyn. **29**, 180 (2015).

[32] N. Gomathi, A. Sureshkumar, and S. Neogi, JSTOR **94**, 1478 (2019).

[33] R. Zhou, X. Zhang, Z. Bi, Z. Zong, J. Niu, Y. Song, D. Liu, and S. Yang, Appl. Environ. Microbiol. **81**, 5257 (2015).

[34] Z. Wan, Y. Chen, S.K. Pankaj, and K.M. Keener, LWT - Food Sci. Technol. **76**, 124 (2017).

[35] N.N. Misra, S. Kaur, B.K. Tiwari, A. Kaur, N. Singh, and P.J. Cullen, Food Hydrocoll. **44**, 115 (2015).

[36] L. Xu, A.L. Garner, B. Tao, and K.M. Keener, Food Bioprocess Technol. **10**, 1778 (2017).

[37] S.K. Pankaj and S. Thomas, *Cold Plasma Applications in Food Packaging* (Elsevier Inc., 2016).

[38] R.S. Brayfield, A. Jassem, M. V. Lauria, A.J. Fairbanks, K.M. Keener, and A.L. Garner, Plasma Chem. Plasma Process. **38**, 379 (2018).

[39] K.M. Keener and N.N. Misra, *Future of Cold Plasma in Food Processing* (Elsevier Inc., 2016).

[40] D. Ziuzina, S. Patil, P.J. Cullen, K.M. Keener, and P. Bourke, J. Appl. Microbiol. **114**, 778 (2013).

[41] F.C. Ekezie, D. Sun, and J. Cheng, Trends Food Sci. Technol. **69**, 46 (2017).

[42] F. Sampedro, A. McAloon, W. Yee, X. Fan, and D.J. Geveke, Food Bioprocess Technol. **7**, 1928 (2014).

[43] M. Laroussi, IEEE Trans. Plasma Sci. **30**, 1409 (2002).

[44] C. Chen, D.X. Liu, Z.C. Liu, A.J. Yang, H.L. Chen, G. Shama, and M.G. Kong, Plasma Chem. Plasma Process. **34**, 403 (2014).

[45] Z.C. Liu, D.X. Liu, C. Chen, D. Li, A.J. Yang, M.Z. Rong, H.L. Chen, and M.G. Kong, J. Phys. D. Appl. Phys. **48**, 495201 (2015).

[46] I. V. Adamovich, M. Nishihara, I. Choi, M. Uddi, and W.R. Lempert, Phys. Plasmas **16**, 113505 (2009).

[47] M. Arif, M. Karl, T.M. Abdel-fattah, and R. Heller, Plasma Chem. Plasma Process. **37**, 59 (2017).

[48] F. Iza, J.L. Walsh, M.G. Kong, and S. Member, **37**, 1289 (2009).

[49] S.K. Park and D.J. Economou, J. Appl. Phys. **68**, 4888 (1990).

[50] D. Burnette, I. Shkurenkov, I. V. Adamovich, and W.R. Lempert, Plasma Sources Sci. Technol. **25**, 025012 (2016).

[51] R.H. Stark and K.H. Schoenbach, J. Appl. Phys. **89**, 3568 (2000).

[52] D.Z. Pai, G.D. Stancu, D.A. Lacoste, and C.O. Laux, Plasma Sources Sci. Technol. **18**, 045030 (2009).

[53] D.Z. Pai, D.A. Lacoste, and C.O. Laux, Plasma Sources Sci. Technol. **19**, 065015 (2010).

[54] D.Z. Pai, D.A. Lacoste, and C.O. Laux, J. Appl. Phys. **107**, 093303 (2010).

[55] M.J. Kushner, J. Appl. Phys. **63**, 2532 (1988).

[56] J. Poggie, N.J. Bisek, I. V Adamovich, and M. Nishihara, in *51st AIAA Aerosp. Sci. Meet. Incl. New Horizons Forum Arosp. Expo.* (Dallas/Ft. Worth Region, Texas, 2013), pp. 1–16.

[57] W.N. Hitchon, T.J. Sommerer, and J.E. Lawler, IEEE Trans. Plasma Sci. **19**, 113 (1991).

[58] J.P. Verboncoeur, Plasma Phys. Control. Fusion **47**, A231 (2005).

[59] R.J. Procassini and C.K. Birdsall, Phys. Fluids B Plasma Phys. **3**, 1876 (1991).

[60] J. Van Dijk, G.M.W. Kroesen, and A. Bogaerts, J. Phys. D. Appl. Phys. **42**, 190301 (2009).

[61] A.K. Verma, A. Alamatsaz, and A. Venkattraman, Plamsa Process. Polym. **14**, 1600130 (2017).

[62] M. Radmilovic-Radjenovic, J.K. Lee, F. Iza, and G.Y. Park, J. Phys. D Appl. Phys. **38**, 950 (2005).

[63] K. Bera, S. Rauf, and K. Collins, IEEE Trans. Plasma Sci. **39**, 2576 (2011).

[64] H.C. Kim, F. Iza, S.S. Yang, M. Radmilović-Radjenović, and J.K. Lee, J. Phys. D. Appl. Phys. **38**, R283 (2005).

[65] J. Poggie, I. Adamovich, N. Bisek, and M. Nishihara, Plasma Sources Sci. Technol. **22**, 015001 (2013).

[66] M.S. Bak and M.A. Cappelli, IEEE Trans. Plasma Sci. **43**, 995 (2015).

[67] D.J. Emmons and D.E. Weeks, J. Appl. Phys. **121**, 203301 (2017).

[68] P.L.G. Ventzek, J. Vac. Sci. Technol. B Microelectron. Nanom. Struct. **12**, 461 (1994).

[69] S.T. Surzhikov and J.S. Shang, J. Comput. Phys. **199**, 437 (2004).

[70] T. Piskin, V. Podolsky, S. Macheret, and J. Poggie, J. Phys. D. Appl. Phys. **52**, 304002 (2019).

[71] G.J.M. Hagelaar and L.C. Pitchford, Plasma Sources Sci. Technol. **14**, 722 (2005).

[72] A. Fiala, L.C. Pitchford, and J.P. Boeuf, Phys. Rev. E **49**, 5607 (1994).

[73] P. Lymberopoulos and D.J. Economou, J. Appl. Phys. **73**, 3668 (1993).

[74] D. Nelson, M. Benhenni, O. Eichwald, and M. Yousfi, J. Appl. Phys. **94**, 96 (2003).

[75] D. Breden and L. Raja, AIAA J. **50**, 647 (2012).

[76] N.H. Chen and D.F. Othmer, J. Chem. Eng. Data **7**, 37 (1962).

[77] T. Deconinck, S. Mahadevan, and L.L. Raja, IEEE Trans. Plasma Sci. **35**, 1301 (2007).

[78] S. Mahadevan and L.L. Raja, J. Appl. Phys. **107**, 093304 (2010).

[79] A. V. Ivanov, S. Trakhtenberg, A.K. Bertram, Y.M. Gershenzon, and M.J. Molina, J. Phys. Chem. A **111**, 1632 (2007).

[80] V. Podolsky and S. Macheret, Plasma Sources Sci. Technol. **28**, 055008 (2019).

[81] V. Paschen, Ann. Phys. **273**, 69 (1889).